Identification and Characterisation of Submesoscale activity over the Continental shelf in the Bay of Biscay

February 2014

Daneeja MAWREN

Dissertation presented in partial fulfillment of the requirements for the co-badged degree of Masters in Ocean and Climate Dynamics shared between the University of Cape Town and Université de Bretagne Occidentale (France)

UNIVERSITY OF CAPE TOWN
IYUNIVESITHI YASEKAPA • UNIVERSITEIT VAN KAAPSTAD

"It is not where you start but how high you aim that matters for success."

Nelson Rolihlahla Mandela (1918-2013)

Dedication

This dissertation is dedicated

to my loving parents,

for their love, encouragement and financial assistance.

to my sister,

for her unflinching support.

Abstract

Frontal instabilities commonly detected in regions of freshwater influence (ROFIs), are considered as fundamental processes in the generation of submesoscale features (a few kilometres to tens of kilometres spatial scale and temporal variability of the order of a day). Consequently, the present study (part of DYMETER project, IFREMER) aims at exploring the development mechanisms of these structures over the continental shelf in the Bay of Biscay. The project is principally based on the analysis of remotely sensed images (high resolution ocean colour MODIS ~800m) of Chlorophyll-*a* concentration, Sea Surface Temperature and Suspended Particulate Matter in view of identifying and characterizing submesoscale activity developing in the vicinity of the Loire River. A 10-year dataset (2003-2013) was explored and satellite ocean colour images revealed a spatial variability in the surface chlorophyll-*a* distribution. In this context, several events on daily, seasonal and interannual scales were selected and compared but the difficulty lies in tracking the continuous evolution of submesoscale structures in time and space due to the presence of clouds obscuring remote optical sensors. Hydrodynamic parameters like wind forcing and river runoffs were also studied to examine their impact on the submesoscale dynamics.

Singularity exponent analysis was performed on the chlorophyll-*a* images to highlight distinct frontal structures which revealed in turn, a multitude of submesoscale fronts and filaments widespread in the upper ocean. The probability density function (PDF-skewness performed on singularity exponents) was used to characterize the submesoscale structures. The analyses carried out showed that during winter, frontal structures gain in intensity due to a high river outflow regime and dominant wind influence. As such, the PDF curve is skewed-right (strong frontal gradient) in winter and skewed-left (weak frontal gradient) in summer. Wavenumber spectrum analysis was also used to characterize submesoscale structures. Slope values ranging between -0.2 to -0.4 were noted but results obtained did not display significant differences in frontal spatial scales with time. Further investigations (beyond the scope of this thesis) will need to be undertaken to evaluate interactions between hydrodynamics and biogeochemistry (using satellite observations and coupled physical-biogeochemical models) for targeted events in the river plumes.

PLAGIARISM DECLARATION

I know the meaning of plagiarism and declare that all of the work in the dissertation, save for that which is properly acknowledged, is my own. Aside from guidance from my supervisors, I have received no assistance, except as acknowledged.

Supervisors:

1. Dr. Guillaume Charria: Laboratoire de Physique Hydrodynamique et Sédimentaire, IFREMER, Brest, France.
2. Dr Jennifer Veitch: Department of Oceanography, University of Cape Town, South Africa
3. Professor Frank Shillington: Department of Oceanography, University of Cape Town, South Africa.

SIGNATURE: 

DATE: ___11th April 2014_____

Acknowledgements

First and foremost, considerable thanks go to my supervisor, Guillaume Charria, for providing invaluable guidance, patience and encouragement throughout the duration of my master's thesis. I truly appreciate all the time and effort he has put in to help me familiarize myself with the Python shell. His continuously good humour and devotion to teach, motivated me to work harder and to be truly invested in the project. He has been a tremendous mentor and I was fortunate enough to have him guiding me through this.

I would like to express my gratitude to Professor Frank Shillington for giving feedback on my chapters and suggesting generality improvements. Many thanks go to Professor Chris Reason for giving me the opportunity to pursue this Master's degree in such prestigious university. This thesis would not have been possible without the Marine Research Institute (Ma-Re) and ICEMASA for their financial support in terms of travel grant and bursary in Brest (France), which broadened my horizons and ideas throughout my dissertation.

I gratefully acknowledge the high performance computing facilities (OPS) at IFREMER, Brest (France) that was available to store large amount of data. I would also like to say a word of gratitude to the staff of DYNECO Lab (IFREMER) for their warm welcome, to the EPIGRAM team and most importantly Xavier Capet, for their useful discussions regarding my work. Interning at IFREMER was really the best experience I have had so far and I will cherish it as one of my most precious memories.

Special thanks go to the Restoration team of IFREMER who introduced to me the culinary and cultural French cuisine as well as the moments I shared with the other postgraduate students during lunch time. I wish to extend my sincere appreciation to my fellow classmates of Ocean and Climate dynamics 2013, South Africa, for facilitating my adaptation to a new country and for their cooperation establishing a pleasant working environment.

Further thanks go to my Mauritian friends, Elodie, Anistah and Azhar for proofreading my work and for always being there with messages of support when needed. There are no words to express how appreciative I am to have met Maggie, Barbara and Avishka for making my stay in

Cape Town a pleasant and memorable one. Last but not the least, I thank my parents for their faith in me and allowing me for being ambitious as I wanted.

Contents

List of Figures

List of Tables

Glossary of Terms

Terms	Definitions
Filaments	Long structures of scales 10 to 20 km across and hundreds of km long that are stretched in between eddies. *(https://ams.confex.com/ams/93Annual/webprogram/Paper221140.html)*
Mesoscales	Energetic structures that are characterized by a spatial scale of 10 to 100 km and time scales ranging from a few days to several months. *(http://www.aviso.oceanobs.com/en/applications/ocean/mesoscale-circulation.html)*
Small-scale features	Structures at small length scales ranging from 0.1 to 100m that contribute to mixing and energy dissipation in the ocean. *(Thomas et al., 2008)*
Baroclinic instability	It is basically the rapid rotation (small Rossby number) of strong stable stratified fluids (large Richardson number). It also refers to a mechanism by which vorticity is created. *(http://en.wikipedia.org/wiki/Baroclinity)*
Ageostrophic currents	These currents work against geostrophic currents in the ocean that counterbalance the Coriolis force and the pressure gradient force. They are mostly present due to other forces like friction or centrifugal force from curved fluid flow. *(http://en.wikipedia.org/wiki/Ageostrophy)*
River plumes	Freshwater outflow from rivers are discharged over the continental shelf and is observed by a distinct colour difference due to the content in particulate matters carried out from the watershed.
Frontogenesis	Generation or intensification of a front or frontal zone.
Eddies	Structures of about 10-100 km in diameter moving in circular patterns. They are commonly known as mesoscale eddies and are important due to their contribution to the lateral transport of heat, momentum, and tracer in the ocean. (*Thomas et al., 2008)*
Geostrophic current	An oceanic flow in which the pressure gradient force is balanced by the Coriolis Effect.
Continental shelf	The extended perimeter of each continent and affiliated coastal plain. *(http://en.wikipedia.org/wiki/Continental_shelf)*
Rossby number (R_o)	It is a dimensionless number with the ratio of the inertial to Coriolis forces for a rotating fluid. $$\mathbf{R_o} = \frac{U}{fL}$$ Where **U** is the velocity scale, f is the Coriolis parameter and **L** is the length scale. In order for the flow to be in geostrophic balance, the Rossby number, $\mathbf{R_o}$, should be sufficiently small (The horizontal scale, **L** should be sufficiently large). *(http://glossary.ametsoc.org/wiki/Rossby_number)*
Stratification	It is the vertical distribution of water masses with different densities. The latter are influenced

	by temperature and salinity where less dense water (warm water) is superimposed on denser water (cold water). *(http://centerforoceansolutions.org/climate/impacts/ocean-warming/water-column-stratafi/)*
Rossby radius of deformation	It is the length at which the rotational effects become as significant as buoyancy or gravity waves effects. *(http://en.wikipedia.org/wiki/Rossby_radius_of_deformation)*
Phytoplankton	Microscopic plants that require chlorophyll and sunlight to live and grow in water.
Richardson number (R)	A parameter that can be used to predict the occurrence of turbulence in a fluid. It is basically the ratio of the density gradient to the velocity gradient. **R = – — / —** Where, **g** is the gravity, **ρ** is the density, **u** is the velocity and **z** is the depth. *(http://www.britannica.com/EBchecked/topic/502698/Richardson-number)*
Euphotic layer	Refers to the upper layer of the water that receives sunlight for the process of photosynthesis essential for the growth of plants.
Phytoplankton subduction/ subsidence	It is the process by which the phytoplanktons are transported downwards by vertical circulation processes or downwelling.
Isopycnal surfaces	Surfaces in the ocean where the potential density remains constant.
Frontolysis	It is the collapse or dissipation of a front.
Potential vorticity	The quantity which is proportional to the vorticity and stratification and follows a parcel of water which can only be changed by frictional processes.
Upwelling	Occurs when Ekman transport moves surface waters away from the coastline so that cooler and nutrient-rich water rises from beneath the surface to replace the water that has been pushed away. *(http://oceanmotion.org/html/background/upwelling-and-downwelling.htm)*
Downwelling	It is the process whereby surface waters converge, enabling the cold (denser) water to sink beneath the warm (less dense) water. However, downwelling regions have low productivity since the nutrient-rich water are carried to greater depths and are not resupplied by the cold water. Therefore, the nutrients are quickly used up by the decay of organic matter. *(http://oceanmotion.org/html/background/upwelling-and-downwelling.htm)*
Thermocline	It is the transition layer between the mixed layer (near surface layer) and the deep water layer. The temperature in the thermocline decreases more rapidly with increasing depth than in the mixed layer and deep water layer where the temperature are relatively steady. (http://ww2010.atmos.uiuc.edu/(Gh)/wwhlpr/thermocline.rxml)

Non-algal Suspended Particulate Matter	It is defined as the difference between the total SPM and the phytoplankton biomass derived from chlorophyll-*a*. *(Gohin et al., 2011)*
Turbidity	It is the cloudiness created by the stirring up of suspended sediments in water.

Acronyms

HDF	Hierarchical Data Format
NetCDF	Network Common Data Form
ROFI	Regions of freshwater Influence
SWODDIES	slope water oceanic Eddies
R_o	Rossby Number
R_d	Rossby radius of deformation
R	Richardson number
MODIS	Moderate Resolution Imaging Spectroradiometer instrument
Rrs	Spectral remote sensing reflectance
OBPG	Ocean Biology Processing Group
HYDRO	Banque Nationale de Données pour l'Hydrométrie et Hydrologie
DFT	Discrete Fourier Transform
FFT	Fast Fourier Transform
PDF	Probability density function
SPM	Suspended Particulate Matter
SST	Sea surface Temperature
IFREMER	Institut Français de Recherche pour l'Exploitation de la MER

Chapter 1 Introduction

1.1 Background

High spatial resolution in recent diverse studies has revealed a multitude of submesoscale fronts and filaments on a lateral scale of a kilometer that are pervasive in the upper ocean *(Thomas et al, 2008, Ferrari et al., 2011)*. The submesoscale regime, intermediate between mesoscales and small-scales, is characterized by a horizontal scale of O (1–10) km, a vertical scale of O (100) m, and a time scale of O (1) day (*Lévy el al., 2012, Capet et al., 2008*). According to *Thomas et al., 2008*, these submesoscale features play a crucial role in the vertical transport of mass, buoyancy and tracers in the ocean's surface. They also serve as a pathway in transferring nutrients and processes from the mesoscales to small-scale features. However, due to the presence of clouds obscuring the satellite images or costly *in situ* surveys, studies carried out to understand frontal dynamics were limited. Some studies (Thomas et al., 2008, Lévy et al., 2012, Capet et al., 2008) however, found out that these submesoscale features arise either from forced instabilities when wind stress is applied to mesoscale features, or from unforced ageostrophic instabilities (baroclinic instabilities in the mixed-layer form eddies less than 10km) or through the process of frontogenesis (formation of density fronts) spawning submesoscale circulations.

Some studies *(Sharples and Simpson, 1993, Lagadeuc et al., 1997)* claim that submesoscale processes occur predominantly due to lateral density gradients *(Thomas et al., 2008)* i.e. in regions of freshwater influence (ROFIs). Consequently, for this study, the Bay of Biscay appears to be a favorable region to study the formation of submesoscale processes in a coastal environment like the Loire River.

1.2 Aims

The aims of this project are to:

(1) Identify distinct submesoscale signatures in the Bay of Biscay, particularly at the mouth of the Loire River by using high resolution ocean color (MODIS).

(2) Study the influence of the winds and river runoffs on the circulation of the plumes; how submesoscale dynamics are generated and how they evolve with time and space.

(3) Apply singularity exponent analysis *(Yahia et al., 2010)* (**see appendix A**) to the chlorophyll-a concentration data in order to sort and highlight the frontal structures over the continental shelf.

(4) Apply statistical methods, like spectral analysis and probability density function to the singularities to characterize the submesoscale features and their temporal variability.

1.3 Thesis Structure

Following a brief introduction in **Chapter 1**, the literature part in **Chapter 2** provides an overview of the Bay of Biscay and its general circulation. The submesoscale features and dynamics put forward by other studies are explicitly defined. The importance of submesoscale features in the ocean's surface is understood as well as the mechanisms contributing in their formation. Finally, the evolution of the river plumes over a seasonal scale were also reviewed.

In **Chapter 3**, the ocean scalars obtained from satellite imagery, the techniques used to extract the data and the statistical methods employed for analysis are explained in much detail.

It is then followed by **Chapter 4** which deals with the results obtained; classified on daily, seasonal and interannual scales.

The discussion part in **Chapter 5** is also sectioned into three parts; daily, seasonal and interannual scales. It basically explains the movement of the river plumes and how the submesoscale structures behave seasonally with the influence of winds and river runoffs. It also compares the results with the literature cited in the text.

The project then concludes by reviewing the objectives put forward and summarizing the results obtained. Some ideas for future works are also illustrated in **Chapter 6**.

Chapter 2 Literature Review

This chapter reviews the current state of knowledge on Submesoscale activities and encompasses the work done on the general circulation and hydrological variables present in the Bay of Biscay. It explicitly describes how forced and unforced instabilities drive submesoscale processes and also how the evolution of river plumes (potential location of submesoscale structures) behave seasonally.

2.1 The Bay of Biscay

The Bay of Biscay (Fig 2.1) is located between the Western boundary of France and the Northern coast of Spain. The continental shelf along the Spanish coast narrows to about 30 km and extends to a maximum of 180km off Brittany. The Armorican shelf (150-180km) expands from the entrance of the English Channel to the South at "Plateau de Rochebonne" from where the Aquitaine shelf (50-150 km) begins and extends down to the Spanish boundary *(Koutsikopoulos and Le Cann 1996).*

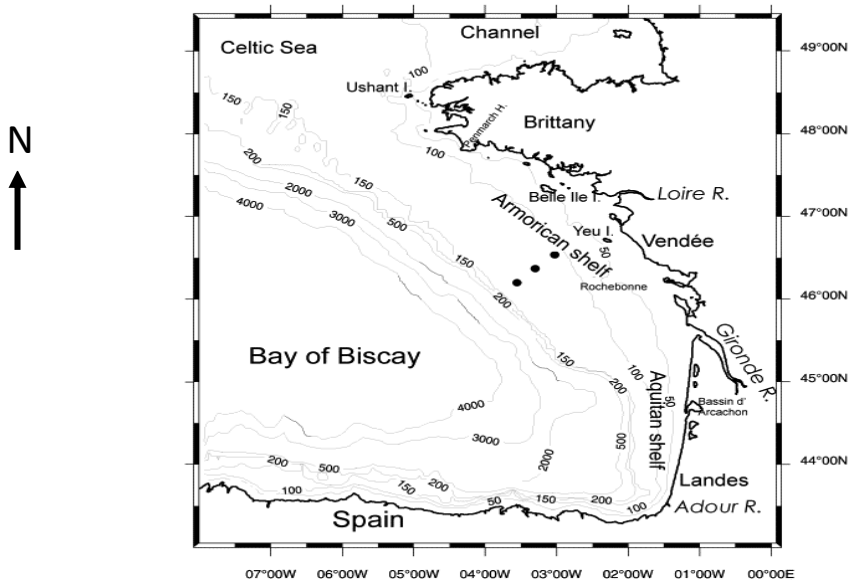

Fig 2. 1 Map of Bay of Biscay (Lazure et al., 2008)

2.1.1 General circulation

The water masses in the Bay of Biscay originate mainly from the Northern branch of the subtropical gyre (Gulf Stream and the North Atlantic Current) (*Koutsikopoulos and Le Cann, 1996)* but also from freshwater discharges from the Loire, Gironde and Adour rivers[1]. As illustrated in Figure 2.2, the general open ocean circulation is oriented in the southern direction and the continental slope current is flowing northwards. However, these circulation patterns display large seasonal fluctuations *(Le Boyer et al., 2013; Charria et al., 2013).* The region midway between Brittany and Southern Spain (illustrated by red dashed box in Figure 2.2) is represented by weak anticyclonic circulation. However, near the continental shelf boundary, the circulation becomes cyclonic with a poleward slope current. The main aspect of this region is characterized by the presence of persistent cyclonic and anticyclonic eddies (called SWODDIES by *Pingree and Le Cann 1992a*), which are generated when the continental slope current instabilities approach the bottom topography (*Koutsikopoulos and Le Cann, 1996)*.

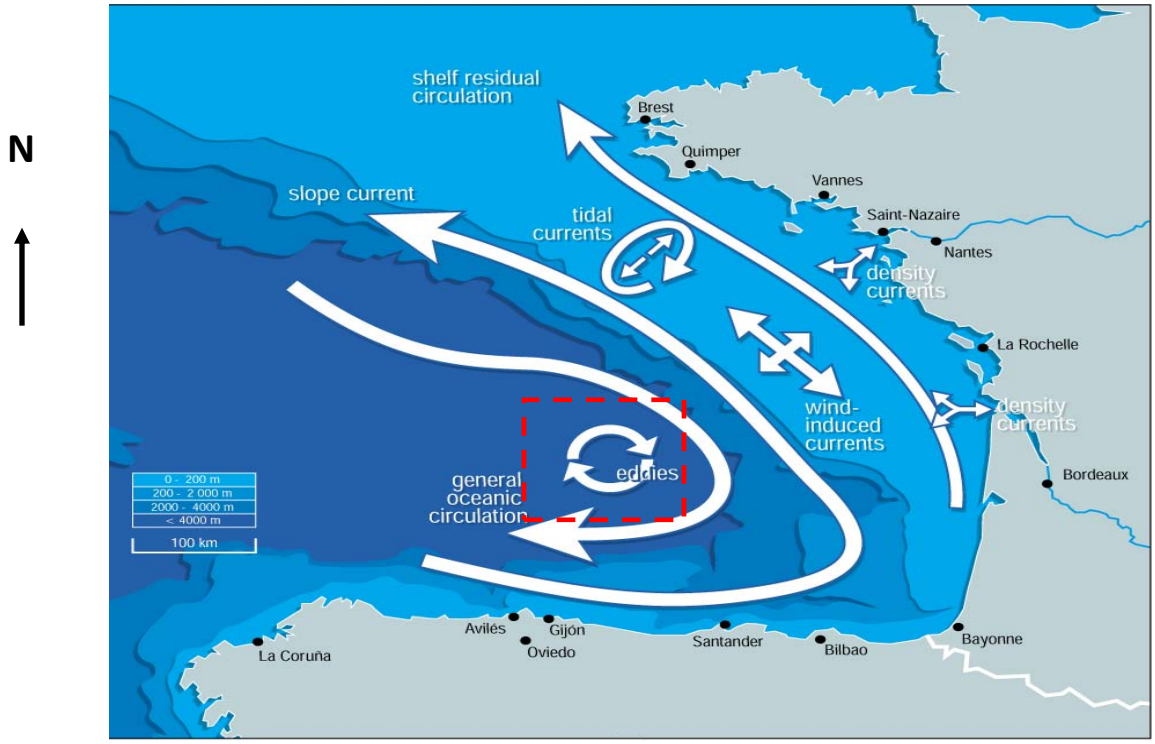

Fig 2. 2 Schematic illustration of circulation in the Bay of Biscay (Koutsikopoulos and Le Cann, 1996/OSPAR)

[1] http://www.eoearth.org/view/article/150448/

According to *Koutsikopoulos and Le Cann (1996),* the mean geostrophic currents are relatively weak (1-2 cms^{-1}) and fluctuating. Residual currents over the shelf are influenced by wind forcing, tides and density gradients (induced by rivers). They also investigated that since the strength of the tidal currents is proportional to the width of the continental shelf, the currents should be very weak in the southern part of the Bay along the French coast. Then in this area, wind and density gradients are the main factors controlling the water masses circulation. Depending on the seasons and wind conditions, the river plumes are normally oriented towards the North due to the Earth's rotation *(Koutsikopoulos and Le Cann, 1996).* Throughout this study, special attention will be devoted between the dynamics of the river plumes and the hydro climatic characteristics (winds, river runoffs) over the continental shelf in the Bay of Biscay.

2.2 Submesoscale processes

Turbulence **(see appendix A.1)** in the upper ocean is ruled by three categories of motions, namely, mesoscale eddies, internal waves and three-dimensional turbulence *(Lévy et al, 2012)*. Latest progress in both observation capabilities and numerical modelling have revealed that the ocean's surface is made up of an overflow of fronts and filaments with spatial scales of a kilometre *(Thomas et al., 2008)*. The fourth type of motion, characterized by O(1) Rossby number (R_o) is known as submesoscale frontal dynamics which lies between mesoscale and small-scale processes *(Lévy et al, 2012)*. A large part of studies on ocean dynamics were based on the analysis of large and fine scale processes but a small part of it was based on intermediate scale (Submesoscales)[2]. More recently, with the advent of high resolution (less than a kilometre) observations and numerical experiments, the important impact of submesoscale processes on the biogeochemistry (*i.e.* new production) has been highlighted.

Mesoscale eddies were found to develop from an instability along the coast whereby wind-driven currents transmit energy from submesoscale fronts in the upper ocean (Capet et al., 2008a). The submesoscale structures are produced through frontogenesis forming upwelled cold filaments that are drawn offshore and twisted in between the mesoscale eddy centres. As such, instabilities at submesoscale fronts are generated. These develop submesoscale meanders and are divided into

[2] http://www.gfdl.noaa.gov/bibliography/related_files/bfk0801.pdf

wrap-up vortices (Capet et al., 2008a). *Lévy et al. (2012)* observed that submesoscale fronts are significantly affected by the rotation of the Earth as well as density stratification as opposed to small-scale turbulence *(Capet et al., 2008a).*

Studies that adopted a numerical resolution not smaller than the baroclinic Rossby radius of deformation (Rd) divided by 4 were able to reproduce explicitly the mesoscale structures compared to the submesoscale features *(Lévy et al., 2001). Spall and Richards (2000)* made use of a resolution of Rd/9 which represented the submesoscales distinctly and in turn enabled them to observe the production of small-scale features in the phytoplanktonic field. *Lévy et al. (2012) and Capet et al. (2008a)* characterized the submesoscale structures in the open ocean by a horizontal scale of 1-10km, which is less than the first baroclinic deformation radius; has a vertical scale of 100m and a temporal variability of the order of days .

Capet et al. (2008b) investigated submesoscale currents in a subtropical and eastern boundary, upwelling regime. A submesoscale shift appeared in the eddy variability when the horizontal scale was reduced to O (1km) as shown in Fig 2.3. It was also proved that when using a better resolution (750m) and when comparing with resolutions where the submesoscale activity is less highlighted, the structure of the submesoscale circulation became much more evident.

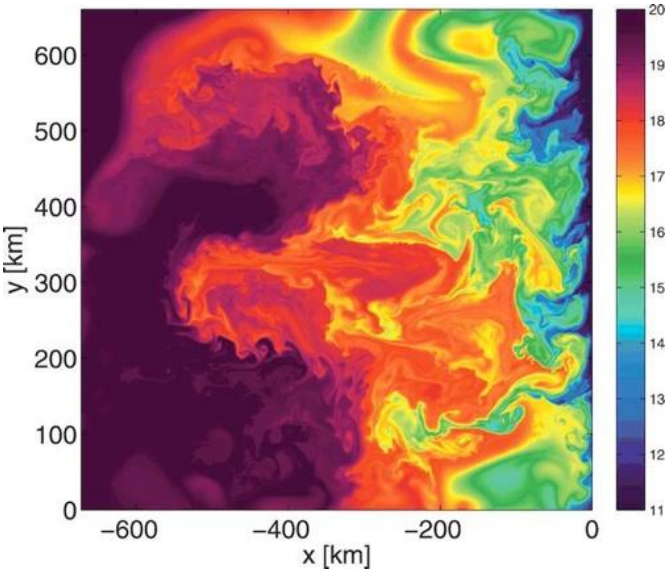

Fig 2. 3 Instantaneous surface temperature T(x,y) field at time t=208 days after initialization as an example of a suite of computational simulations for an idealized subtropical, eastern boundary, upwelling current system [referred to as the idealized California Current (ICC)] (Capet et al., 2008b)

It was noted that high resolution observations and simulations yield interesting and distinct features of submesoscale structures. Some previous studies have applied statistical analysis to these resolutions to characterize the submesoscale features. *Charney (1971)* claimed that mesoscale stirring would actuate a forward entropy cascade *(transfer of kinetic energy from large through successively smaller scales dissipating thermal energy)* in accordance with a kinetic energy spectrum of slope k^{-3} (**see appendix A.2**). Satellite images *(Gower et al., 1980)* brought out spatial variability in the surface chlorophyll distribution at scales ranging between 5 and 20 km for submesoscale features. Spectrum analysis (*Gower et al., 1980)* implemented on sea surface chlorophyll images displayed k^{-3} slopes intermediate between mesoscale and submesoscale and they proposed that submesoscale features were weaker than mesoscale structures *(Lévy et al., 2001)*. Numerical experiments in the oceanic framework have shown that the quasi two-dimensional mesoscale flow field is identified by a kinetic energy spectra slope of k^{-3} *(Capet et al., 2008a; Capet et al., 2008c and Klein et al., 2007)*. However, satellite images with progressively increased spatial resolution unveiled a k^{-2} spectral slope denoting that submesoscale structures were much more dynamic *(Denman and Abbott., 1994)*. 3D numerical simulations with increasing resolutions also made it clear that resolving submesoscale processes reduces the kinetic energy slope to k^{-2}*(Capet et al., 2008a; Capet et al., 2008c; Legg and McWilliams, 2001)*.

Both observations and simulations were able to prove that submesoscale activities occur widely in the upper ocean. At meso and larger scales, where most of the ocean's kinetic energy is stored, it is however hard to extract energy since the system is in geostrophic equilibrium. Hence, submesoscale processes [Rossby number, Ro and Richardson number, R of O(1)] with associated vertical velocities of $O(10^{-3}$ m $s^{-1})$ *(Thomas et al., 2008)* play a fundamental role in the vertical transport of mass, buoyancy and tracers in the near-surface. At ocean fronts, intense vertical velocities can lift the nutrients beyond the mixed layer to the surface layer causing an increase in the ocean's productivity. If the vertical mixing at submesoscale fronts is reduced, this can locally increase the average time that the organisms spend in the clear euphotic layer and on that account contribute to primary production *(Lévy et al., 2012)*. Consequently, submesoscale processes serve as a pathway in the transfer of energy and properties from the mesoscales to small-scales *(Boccaletti et al., 2007)*.

Wang (1993) and Spall (1995; 1997) have carried out investigations on the rate at which submesoscale features are formed and identified their associated strong vertical ageostrophic circulation. Hence, it is believed that the ageostrophic movements associated with these small-scale energetic features can influence new production and phytoplankton subduction.

2.3 Submesoscale sources

So far, the term submesoscale has been defined and its associated phenomena clearly elaborated. The importance of submesoscale processes in carrying energy from mesoscale to small-scale features has been understood. Furthermore, the different processes triggering submesoscale structures in the surface layer are considered.

Recent advances on submesoscale processes are based on different classes of frontal dynamics: wind-front interactions *(Thomas, 2005),* frontogenesis *(Lapeyre et al., 2006, Capet et al., 2008b)* and frontal instabilities *(Boccaletti et al., 2007). Thomas et al., 2008* have put forward a synthesis of surface boundary-layer submesoscale processes that arise in the presence of lateral buoyancy gradients. They characterized their formation through *frontogenesis, unforced instabilities, and forced motions.*

2.3.1 Frontogenesis

Submesoscale frontogenesis evolves in regions where the buoyancy field is under high stress and these regions are normally associated with the edges of mesoscale eddies having large buoyancy gradients and velocities (*Jacobs et al., 2013*)[3]. *Lévy et al. (2012) and Capet et al. (2008a)* observed that submesoscale fronts are more likely to take place at the ocean's surface rather than in the ocean's interior. This is because in the ocean's interior, the density surfaces are relatively flat with slope less than O(Rossby number). Therefore, when a large-scale velocity field acts to steepen the density surfaces, an overturning circulation is built up bringing the surfaces back to their horizontal position, hence re-establishing the geostrophic balance. This explains why submesoscale processes with Rossby number, Ro = O(1), do not occur readily in the ocean's

[3] https://ams.confex.com/ams/93Annual/webprogram/Paper221140.html

interior. Hence, the horizontal circulation operates in such a way to further accentuate the convergence of density surfaces resulting in the formation of sharp density fronts known as *frontogenesis* (Fig 2.4). As the fronts develop, the steepness of the density surfaces rises and Rossby number, Ro is shifted to O(1). This therefore leads to strong ageostrophic submesoscale circulations producing energy to excite the microstructure turbulence *(Lévy et al., 2012).*

Satellites images *(Munk et al., 2001)* and *in situ* observations *(Rudnick, 2001)* both agree that the ocean is full of eddies with characteristics in accordance with the submesoscales. Both mesoscale eddies and submesoscales drive overturning circulations that act to collapse lateral density gradients, converting sharp isopycnal surfaces to shallower and unstable ones. This results in a lateral mixing of tracers and an increase in the vertical density stratification. During this process, lighter water is moved over denser water and potential energy is extracted *(Fox-kemper et al., 2008b).*

Capet et al., 2008a found out that mesoscale eddies originate from wind-driven currents and coastal instabilities. By the process of frontogenesis, the amount of energy dissipated due to mesoscale strain is transferred into the submesoscale fronts in the surface boundary layer. This therefore leads to submesoscale frontal instabilities and develops submesoscale meanders *(Capet et al., 2008a).* A parameterization scheme for numerical modelling has been developed by *Fox-Kemper et al., 2008a* and Fox-kemper and Ferrari (2008) to reproduce the mixed-layer restratification associated with frontal instabilities and frontogenesis. They observed that submesoscale dynamics are dominated by the development of fronts and ageostrophic circulations associated with fronts. The small stratification and low depth of the mixed layer induce submesoscale ageostrophic baroclinic instabilities that are enclosed within the mixed layer. The change in stratification and the flux of potential vorticity to and from the surface to the interior ocean is the other factor that characterizes submesoscale instabilities. Submesoscale instabilities in the mixed layer actually boost the restratification and buoyancy transport in comparison to mesoscale baroclinic instability *(Fox-Kemper et al., 2008a).*

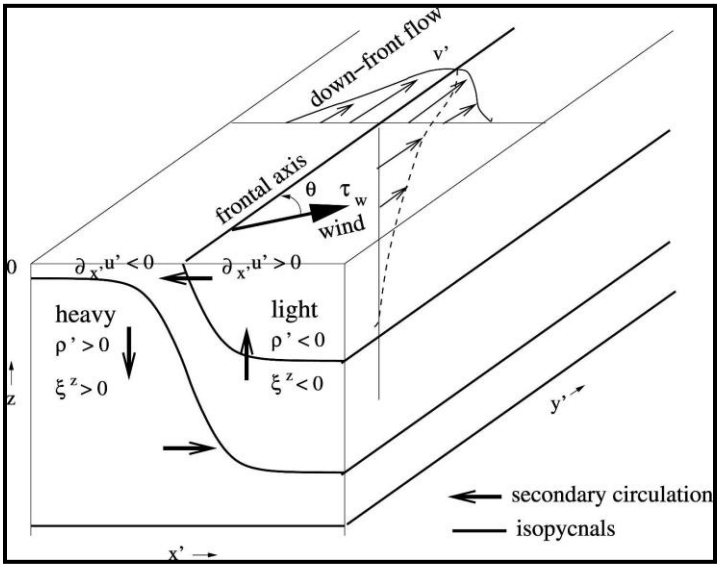

Fig 2. 4 Schematic configuration for an intensifying straight surface front with f > 0; (x*,y*) and (u*,v*) are rotated horizontal coordinates and velocity aligned with the frontal axis and its approximately geostrophic jet flow and δρ is the local potential density perturbation. Also shown is the orientation angle θ relative to the surface wind stress. (Capet et al., 2008b)

Submesoscale fronts usually last only a few days after they are formed. This is due to the instability of the fronts or because the convergent flow stops (frontolysis) as currents and mesoscale eddies develop. Frontolysis (frontal collapse) is generally caused by winds (*Thomas, 2005*). Winds blowing in the opposite direction of the frontal currents may cause the front to collapse therefore accelerating restratification by frontal instabilities. During frontolysis, the vertical velocity and the exchange of properties with the ocean interior gradually decrease. This drop is further accentuated when frontolysis is associated with frontal instabilities, taking often a few hours *(Lévy et al., 2012).*

2.3.2 Unforced instabilities

Boccaletti et al. (2007) showed that baroclinic instability arises at the mixed-layer Rossby radius of deformation, R_d, developing eddies of size L = (1 – 10) km which are called ageostrophic instabilities. The timescale of Mixed Layer Instability (MLI) is shorter than that of the mesoscale baroclinic instability and the former accelerates the collapse of the fronts leading to a fast restratification of the mixed layer. As submesoscale meanders develop, lighter water superimposes onto the denser side of the front and as the frontal outcrop is forced back, the front

collapses and the mixed layer restratifies. Values of R_o during the evolution of the mixed layer regime denote that the instability is greatly influenced by the ageostrophic component of the flow *(Thomas et al., 2008).*

2.3.3 Forced Motions

Submesoscale turbulence can also be generated when atmospheric forcing (heat, salt fluxes or wind stress) is applied to baroclinic mesoscale features. This phenomenon leads to a reduction in the stratification, Richardson number, R and, typically, potential vorticity of the upper ocean (*Thomas et al., 2008*).

(i) Buoyancy loss

When a homogeneous layer is cooled laterally, this may generate submesoscale instabilities. As such, a lateral buoyancy gradient produces a baroclinic jet through geostrophic adjustment *(Haine and Marshall (1998)* as cited in *Thomas et al., 2008). Yoshikawa et al. (2001)* proved that a change in the buoyancy flux at an ocean front can increase the frontal vertical circulation. They also observed that lateral stress associated with baroclinic instabilities was more intense for fronts forced by cooling in comparison to unforced motions and resulted in more energetic frontogenesis.

(ii) Down-front Wind stress

Stratification and Richardson number are decreased in the surface layer when winds blow in the same direction as the surface frontal jet (Down-front Wind). This therefore triggers submesoscale processes *(Thomas and Lee, 2005).* In this case, denser water overrides the less dense water causing instability in the water column and stimulating convective mixing *(Thomas and Lee 2005).* The mixing power depends on the strength of the surface lateral buoyancy gradient and on Ekman transport. *Thomas et al. (2008)* observed through simulations that a down-front wind blowing over a frontal jet will advect surface Ekman transport from the dense to less dense part of the front. Secondary circulation with convergence and downwelling on the dense side of the front and divergence and upwelling at the centre of the jet are induced when the Ekman transport is weaker on the cyclonic side of the jet and vice versa.

2.4 Evolution of River Plumes in the Bay of Biscay

The present study aims at identifying and characterizing the submesoscale dynamics over the continental shelf in the Bay of Biscay. Firstly, observations and density gradients suggest that frontal activity on the shelf is located in the Region Of Freshwater Influence (ROFI). On that account, our study is to focus on the turbulence induced by river plume dynamics.

A 3D model of the Atlantic shelf has been put forward by *Lazure and Jégou (1998)* to study the shelf dynamics and observe the evolution of fresh water discharges of the Loire and Gironde rivers during winter and spring seasons. Simulations performed over 7 years have shown that the evolution of plumes is mainly driven by winds and the large variability of river runoff.

They observed that during winter, particularly when river runoff is high, the movement of plumes is usually oriented northwards and is confined along the coast. This is because southwesterly winds are more dominant from autumn to early spring *(Le Cann and Pingree, 1995)* causing a fast response of shelf waters. However, from spring to late summer, north-westerly winds actuate south-westerly surface currents over the continental shelf. This may inhibit or reverse the circulation of the plumes towards the south, dispersing low-salinity waters offshore. *Lazure and Jégou (1998)* observed that during winter and spring, cold waters from the Loire, Gironde and Adour estuaries usually cover a wide part of the continental shelf. The same situation is usually observed in summer but with higher salinity water covering a wide part of the continental shelf due to low river runoffs compared to spring (low salinity advected offshore due to high river runoffs). This variability has been proved through the observation of *in situ* measurements *(Puillat et al., 2004, 2006).*
Especially in coastal areas, wind appears to be the main forcing element of long-term transport *(Koutsikopoulos and Le Cann, 1996).*

As determined by *Le Cann and Pingree 1995*, North-westerly winds being parallel to the coast, produce the largest vertical currents compared to westerly or south westerly winds. Due to variations in depth and land influences, wind-driven circulation is complicated alongshore. Close to the Loire estuary, upwelling arises under two different situations due to the coastline

orientations being NW-SE (represented by arrows in Figure 2.5): Northwesterly winds generate upwelling South of the Loire and Westerly winds induce upwelling to the north of the Loire along the Brittany coast (*Lazure and Jégou, 1998*). However, other rivers like Adour and Vilaine are less dominant but the amount of runoff is still important.

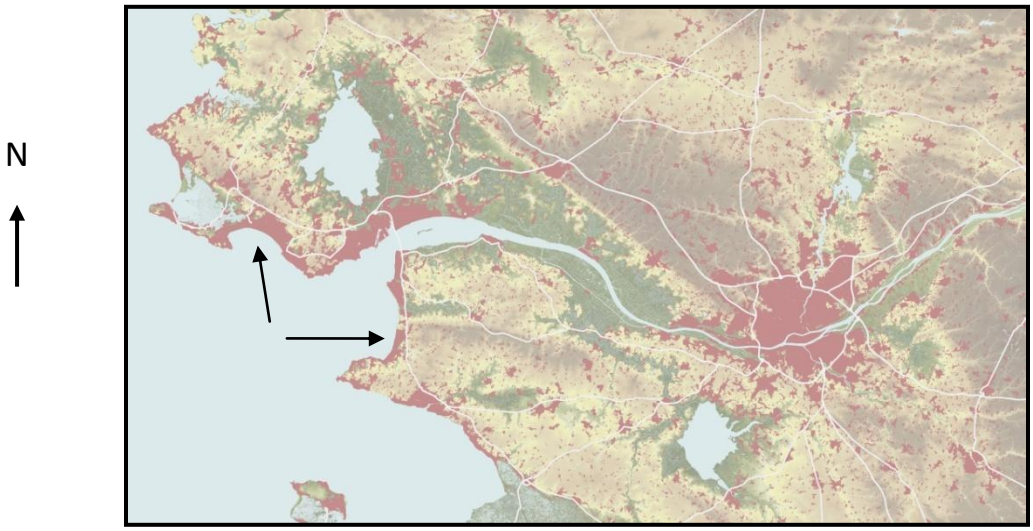

Fig 2. 5 The Loire estuary. The two arrows indicate upwelling taking place in the NW and SE of the river mouth due to the coastline orientations. ***(http://switchboard.nrdc.org/blogs/kbenfield/from_elephant_to_estuary_does.html)***

Loire and Gironde are the two main rivers in the Bay of Biscay having the highest runoffs in winter with an annual mean outflow of about 900m^3 s^{-1}, often attaining 3000m^3 s^{-1} *(Lazure and Jégou, 1998).* Salinity gradients are usually very high at the estuary mouth due to freshwater discharges and they form a surface-layer plume with currents oriented downstream at the surface and upstream at the bottom. The water originating out of the estuary has a lower density than the surrounding waters. This develops a pressure gradient, which causes the plume to spread laterally towards the right (northern hemisphere) due to the earth's rotation *(Lazure and Jégou, 1998).* Model simulations made by *Jégou and Lazure (1995)*, showed that baroclinic coastal currents occur predominantly due to density gradients caused by the river discharges and the spreading of plumes depends largely on wind stress. They concluded that the evolution of river plumes is driven by seasonal forcing events: usually highest runoff and downwelling-favourable winds in the winter season whilst decreased runoff and upwelling-favourable winds occur in spring.

As observed by *Koutsikopoulos and Le Cann, (1996)*, during winter and spring, cold waters from the Loire, Gironde and Adour estuaries cover a large part of the continental shelf. This low salinity water accounts for the inversion of the temperature vertical profiles and presence of strong vertical gradients. During April, the seasonal thermocline develops in the western part of the shelf and reaches the coastal zone around May. While monitoring the thermocline, *Vincent and Kurc (1969)*, identified a cold pool called "Bourrelet Froid", which expands from Southern Brittany to the Gironde estuary. This structure appears the whole year with a temperature gradient of less than 1 °C from spring to autumn. *Le Cann (1982)* observed that the development of the "Bourrelet froid" (figure 2.6) is impeded by freshwater discharges principally for areas close to river plumes. Particularly in autumn, a warm pool (warm water tongue) is developed alongshore between the Loire estuary and the southern part of the Bay denoted by number 9 in Figure 2.6 *(Vincent and Kurc, 1969)*. According to *Le Cann (1982)*, the formation of this warm water mass arises due to mixing of tidal and wind induced currents as well as the ocean-atmosphere thermal exchanges.

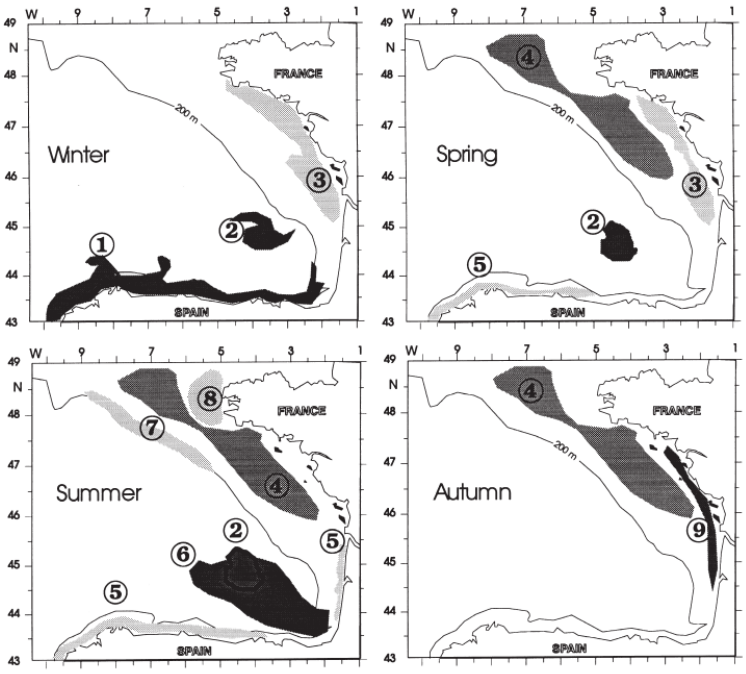

Fig 2. 6 Hydrological structures in the Bay of Biscay: 1) winter warm current, 2) Swoddies, 3) river plumes, 4) cold water masses 'Bourrelet froid", 5) Upwelling, 6) Warm waters of the Bay, &) Slope fronts, 8) Tidal fronts, 9) Warm water tongue "langue d'eau chaude". (*Koutsikopoulos And Le Cann, 1996)*

Chapter 3 Data and Methods

With the objective of identifying the submesoscale structures in the Bay of Biscay, different observed parameters have been analyzed and different methods have been applied to the data to characterize these features.

3.1 Remotely sensed data

The present study has been based on observations collected by the Moderate Resolution Imaging Spectroradiometer (MODIS) instrument. MODIS on board Aqua and Terra satellite platforms captures data of the Earth's surface each 1-2 days with a swath width of 2330 km. The sensors cover 36 spectral bands with wavelengths ranging from 0.405 to 14.385 μm [4] and retrieve data products at varying spatial resolutions – 250 m, 500 m and 1000 m.

3.1.1 Chlorophyll-a concentration

Chlorophyll-*a* concentration is commonly used as an index of phytoplankton biomass in the surface layer of the water. Ocean colour sensors provide the only way for observing a wide spatial distribution of phytoplankton in the ocean by absorbing and scattering light striking the water.

After the natural death of a phytoplankton, chloroplasts release the active chlorophyll. Fluorescence is used to estimate the phytoplankton Chlorophyll concentrations. The objective is to illuminate it by an ultraviolet light of wavelength around 430nm and light emitted by the fluorescence is measured at wavelength around 669nm (Figure 3.1). The detection is made by a photodiode that generates a current proportional to the light received in the spectrum range to which it is sensitive. This current is converted to voltage and amplified in order to be read by the data acquisition card.

[4] *http://modis.gsfc.nasa.gov/data/*

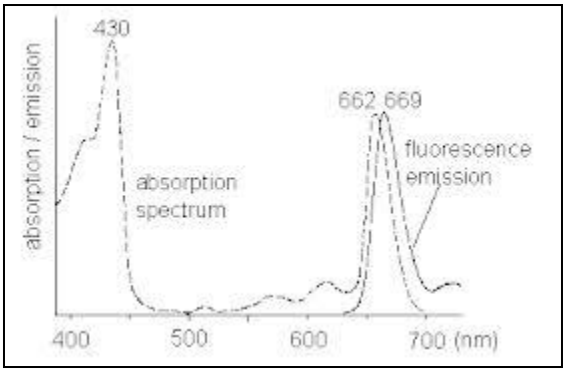

Fig 3. 1 Absorption and emission spectrum of chlorophyll-a (*http://www.photosynthesis.ch/fluorescence.htm)*

Satellite images of chlorophyll-*a* concentration from MODIS are retrieved for a period of 10 years with a Spatial Resolution of 800 m. In order to process the MODIS data for retrieval of Chlorophyll-*a* concentration, a bio-optical empirical algorithm known as the Five-Channel algorithm (OC5) developed by *Gohin et al., 2002* is used for case 2 French Coastal waters. This algorithm actually adjusts the overestimation of chlorophyll-*a* concentration in turbid waters by making use of a lookup table suited for the French Northern Coastal waters based on the Spectral remote sensing reflectance (Rrs) of 555 nm and 412 nm. This gives similar results to Ocean Colour 4 in open waters but provides more reasonable results over the continental shelf. For this study, satellite images of the chlorophyll-*a* concentration were investigated for a period of 10 years (2003-2013).

3.1.2 Sea surface Temperature

Sea Surface Temperature (SST) data are sourced from MODIS on the NASA Earth Observing System satellites Aqua and Terra [5]. MODIS measures the radiance in the infrared band around two wavelengths: 3.9 µm and 11 µm so that the surface temperature of the ocean can be derived. Level 2 products provide SST data at a resolution of about 800 m and cover the whole globe during daytime and nighttime on a daily basis. The SST data derived from high resolution satellite measurements are used to locate SST frontal variability. NASA standard processing and

[5] *http://oceancolor.gsfc.nasa.gov/cgi/browse.pl?sen=am*

distribution of the SST products from the MODIS sensors are completed using the Ocean Biology Processing Group (OBPG). It initiates the Level-2 SST products using the Multi-Sensor Level-1 to Level-2 Software (msl12), which is the same software used to generate the MODIS ocean colour products [6]. Satellite data are typically distributed and downloaded in HDF file format. They are then converted to NetCDF format using a Matlab program where SST maps are in turn visualised using a Python program. Unlike for chlorophyll-a concentration where the images were analyzed for the whole dataset (2003-2013), satellite images of SST were retrieved and investigated only for some selected events.

3.1.3 Non-algal Suspended Particulate Matter concentration

Non-algal Suspended Particulate Matter (SPM) is obtained by calculating the difference between the Total SPM and Chlorophyll-a concentration (Phytoplankton biomass). SPM is significant over the continental shelf because its properties determine turbidity in the water column which restricts primary production and impacts on the transfer of heat. The spatial and temporal variability of the SPM in surface waters are analyzed with a spatial resolution of 800 m and a daily temporal resolution. Images of non-algal SPM concentrations are derived from MODIS AQUA L2 satellite data *(Rivier et al., 2012)* using the IFREMER semi-analytical algorithm *(Gohin et al., 2005)* and the data are retrieved for a period of 10 years (2003-2013). This method actually extracts non-algal SPM from remote-sensing reflectance and is based on the reversal of the radiative transfer equation, which applies the 670mn instead of the 550nm (initial algorithm) whenever the SPM exceeds 4 mg/L.

3.1.4 Winds

In order to study the impact of the winds on the circulation of the river plumes and to explain the change in the intensity of the frontal structures, wind data are extracted for a period of 8 years (2006-2013) from the numerical weather model called ARPEGE from Météo France (Déqué et al., 1994). The model covers the entire globe with a horizontal resolution of 0.5° over France. To generate the wind maps, a 6 hourly temporal resolution was used.

[6] *http://oceancolor.gsfc.nasa.gov/DOCS/modis_sst/*

3.1.5 River runoffs

The data centre for French coastal operational oceanography (CDOCO) collects freshwater input such as river flows and rate of precipitation, which are *in situ* measurements. They are received from near real time and from several measurement networks. It provides a list of French rivers, their time series and corresponding distributors. For this study, data for the Loire River were collected for the analyzed dataset (2003-2013) via Banque HYDRO (*Banque Nationale de Données pour l'Hydrométrie et l'Hydrologie*) which measures effectively at each station the instantaneous river runoffs. These are recovered on a daily basis. The data are stored and distributed in NetCDF format.

3.2 Data availability

Before applying the methods to the ocean scalars, the 10-year chlorophyll-*a* concentration dataset was analysed visually to classify only cloud-free images. It was observed that there were very few clear images for investigation which result in the difficulty of tracking the formation of submesoscale structures over a temporal scale of days. Figure 3.2 shows that the number of cloud-free images does not exceed 60 images per year and it also indicates a decreasing trend with time. This decrease is not fully explained and would need further investigations, out of the scope of the present study. This time series also highlights interannual fluctuations in the number of cloud free images as observed in Figure 3.3. This can be directly correlated with the weather regime during these years (see section 4.4). Year 2003 and 2005 are classified among the driest years due to their higher number of cloud-free images in comparison with 2009 and 2011 categorized as the wettest years.

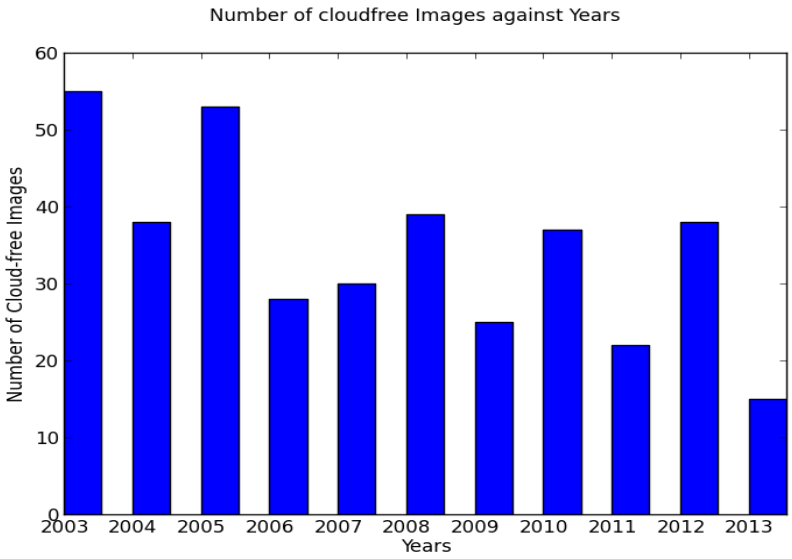

Fig 3. 2 Availability of cloud-free images for a period of 10 years.

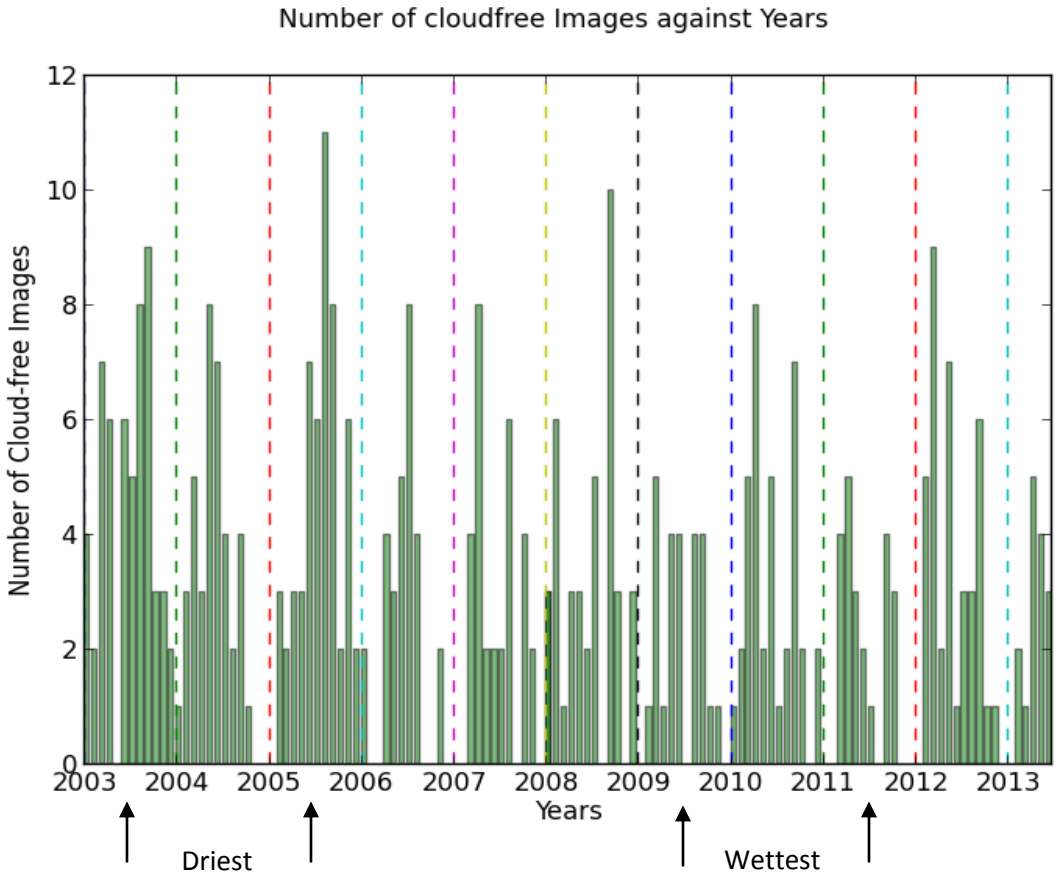

Fig 3. 3 Number of cloud-free images plotted on a monthly basis for a period of 10 years.

3.3 Methodology

Based on the limited number of cloud-free images, some methods were put forward to highlight, sort and characterise the submesoscale structures.

3.3.1 Singularity exponents

Singularity analysis is the process of calculating the degree of regularity or irregularity of a function at each point in a domain [7]. The purpose is to acquire a dimensionless quantity at each domain point and is called the singularity exponent. Throughout this study, the analysis of the Singularity exponents is applied to remotely sensed Chlorophyll-*a* concentration data only in view of identifying and highlighting frontal structures. The singularities revealed a convoluted network of fronts and filaments in a more detailed way. It can be calculated from any other ocean parameter (Sea Surface Height, Sea Surface Salinity, SST) and should give similar singularities as it is a consequence of flow advection. (*Isern-Fontanet et al., 2007; Nieves et al, 2007)*

The theory is explained in detail in *Turiel et al. (2008)*, where the singularity exponent is considered to be an extension of differentiation, in which the degree of regularity of a signal s at a point **x** is measured by the Hölder exponent, H(**x**) at that point (see Appendix B). *Turiel et al. (2003) and Turiel & Parga (2000)* calculated the modulus of the gradient of the ocean scalar at each domain point and projected it on a wavelet at different scales. They observed that the singularity exponent was represented precisely with a better spatial resolution. Negative values of Singularities indicate that the signal is not regular or discontinuous and encounters abrupt shifts (stronger frontal activity) while positive singularity exponents (weak frontal activity) denote continuous signals (figure 3.4) (*Turiel et al., 2008*).

Before generating images of singularity exponents, a python program was first implemented to fill in the missing values present in the chlorophyll-*a* concentration data by the mean of chlorophyll-*a*. Then, images have been processed by J. Sudre (LEGOS, Toulouse) using the software co-developped by H. Yahia (INRIA, Bordeaux) and J. Sudre (Yahia et al., 2010).

[7] *http://cp34-bec.cmima.csic.es/new-singularity-exponent-products-now-available/*

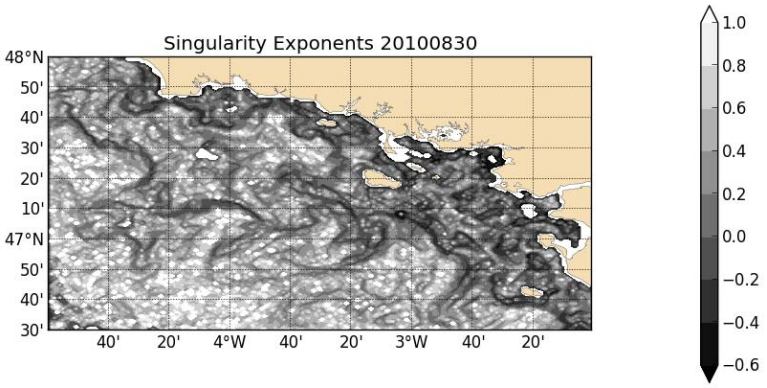

Fig 3. 4 Singularity exponent imagery taken on the 30th August 2010 showing frontal structures alongshore.

3.3.2 Fourier Analysis

The second method used in this study is the Fourier transform which is based on the decomposition of a function into sinusoidal components. The Fourier transform of f(x) is defined by the equation:

$$F(s) = \int_{-} f(x)e^{-i2\pi sx}\, dx \quad \text{, where s is the frequency.} \qquad \textbf{(1)}$$

The inverse Fourier transform is given by:

$$F(x) = \int_{-} f(s)e^{i2\pi sx}\, ds \qquad \textbf{(2)}$$

Discrete Fourier Transform (DFT) is an approximation of the continuous Fourier transform and is obtained when the function and its Fourier transform are replaced by discretized corresponding values. The estimation of DFT is processed through the Fast Fourier Transform (FFT) which is one of the most important algorithms in signal processing. The FFT decomposes an image at a significantly higher pace into components of different spatial frequencies.

A series of steps were carried out in order to generate the Fourier transform of a given image.

(1) A Chlorophyll-*a* concentration image has been selected.

(2) A smaller domain (Latitudes: 46.3N to 47.1N and longitudes: -2.3W to -4.5W) was chosen whereby land pixels were excluded and the interpolation was done over ocean

areas only (Figure 3.5).

(3) The Fourier analysis was carried out for all latitudes (Horizontal strips in Figure 3.5) and longitudes, both generating the same spectral slope.

(4) A Power spectral density curve was plotted for all the latitudes (represented as blue curves in figure 3.6) and the mean was also computed (represented as red curve in figure 3.6) and used throughout the whole study.

(5) When performing the Fourier transform on the Singularity exponent imagery, it was observed that the spectral energy was higher compared to that of Chlorophyll-*a* concentration. This is because the frontal structures were accentuated and hence generating a higher energy.

(6) Finally, the Fourier spectrum was plotted on a log-log graph with spatial frequency on the x-axis and the Power Spectral Density (PSD) on the y-axis (Figure3.6). The power spectrum of a signal is a function giving the power of the signal as a function of frequency or wave number.

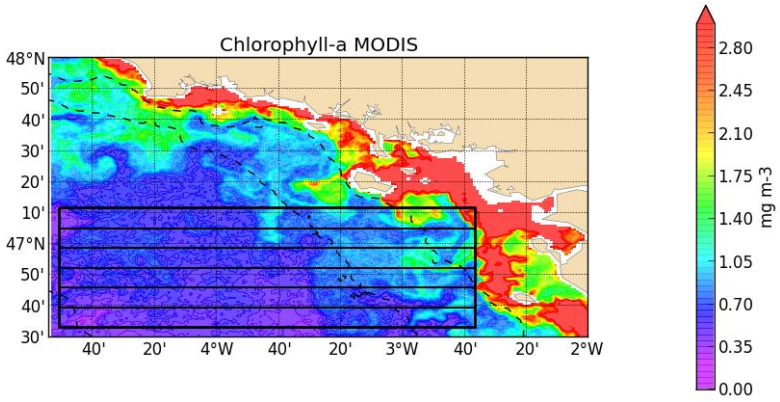

Fig 3. 5 Chlorophyll-*a* image showing the selected zone used to perform the Fourier transform

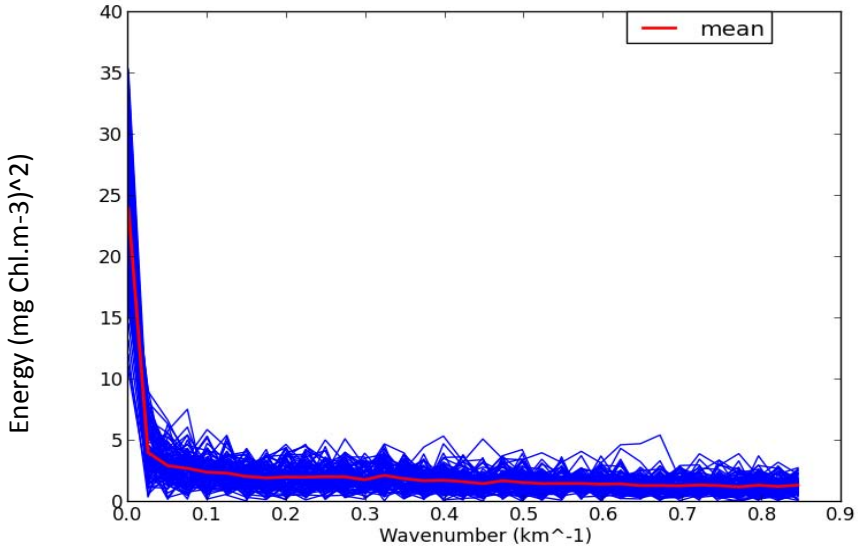

Fig 3. 6 Fourier transform performed along all the latitudes. Red curve represents the mean power spectrum.

3.3.3 Probability Density Function

Probability Density Function (PDF), also termed Probability Distribution Function, of a random variable is defined as the probability of finding a value over a particular range of the variable. It is the third method applied to characterise submesoscale features. The PDF of a continuous random variable, Z, is a function f (z) given by the equation below, where f (z) refers to the density curve:

$$P(x_1 \leq Z \leq x_2) = \int_{x1}^{x2} f(z)\, dz \qquad \textbf{(3)}$$

Equation (3) implies that the probability that Z takes a value between x_1 and x_2 is the area under the curve. A histogram is an approximation of the PDF and it is the best and preferred way to represent data graphically. When the number of bins is bigger and smaller, the histogram approaches the probability density function and a smooth PDF curve is then drawn to approximate the distribution (Figure 3.7).

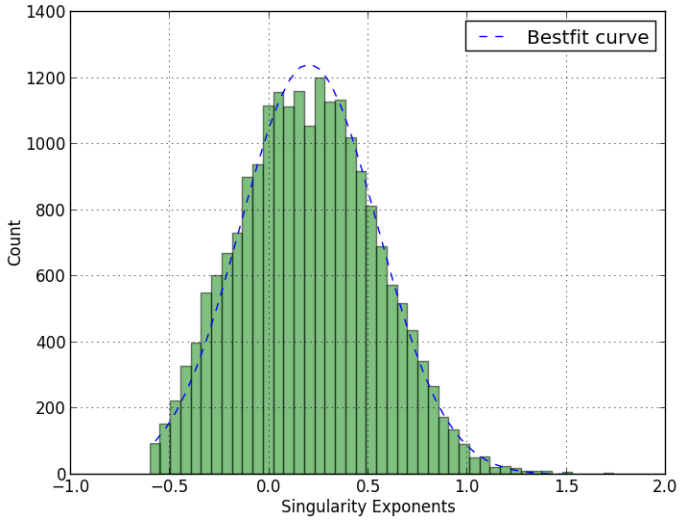

Fig 3. 7 Probability density function represented by a Histogram where the blue curve corresponds to the best fit curve.

The probability density function curve is plotted based on the singularity exponent data and the above figure will indicate whether the graph is skewed, i.e. whether the distribution is clustered more towards one direction than the other. A distribution is said to be positively skewed or skewed-right when the right tail is more pronounced relative to the left and that the mean is greater than the mode while negatively skewed or skewed-left is when the long tail is on the left side of the peak and the mean less than the mode as shown in figure 3.8 [8]. In our study, when the graph is skewed-right, it implies that there are more values in the lower part of the distribution (negative singularities) and therefore it explains the presence of stronger frontal structures and vice versa for skewed-left.

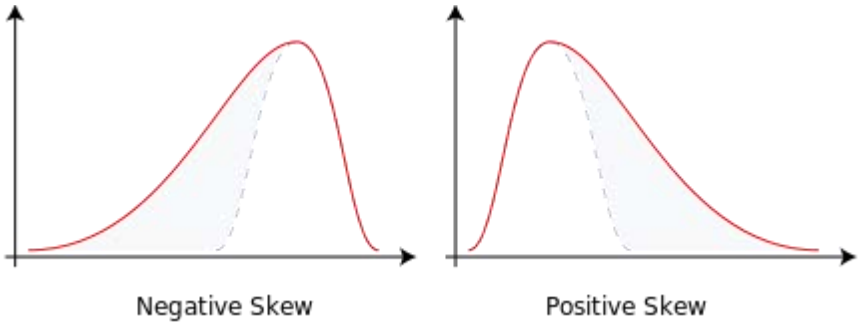

Fig 3. 8 Diagrams illustrating the negative and positive skewness.

Source: Rodolfo Hermans (Godot) (*http://en.wikipedia.org/wiki/Skewness*)

[8] *http://en.wikipedia.org/wiki/Skewness*

Chapter 4 Results

This chapter reports the results of the study focused principally on the Loire River. The primary objective of this research is to identify submesoscale activity, applying different methods described in Chapter 3 to characterize these features. The evolution of the plumes in the region of freshwater influence was also analyzed in terms of spatial and temporal scales using satellite images of Chlorophyll-*a* concentration as a proxy for monitoring the dispersion of phytoplankton biomass. An attempt was also made to investigate the influence of river runoffs and wind conditions over the submesoscale regime in this region.

4.1 The Study Region

The domain selected in Figure 4.1 (right) lies between latitudes 46.5^{o}N and 48^{o}N and longitudes 2^{o}W to 5^{o}W. It covers the mouth of the Loire estuary and extends about 150 km cross shore. This region was kept fixed throughout the whole study.

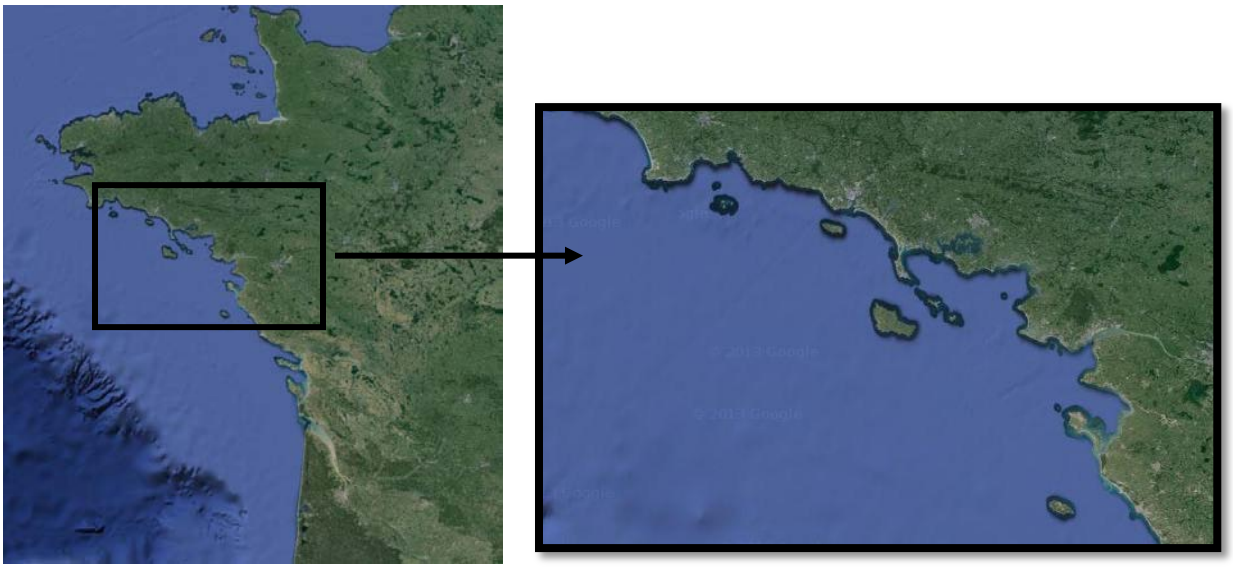

Fig 4. 1 Location of Loire river in the Bay of Biscay (left) and area of study (right) (*Source: https://maps.google.co.za/)*

4.2 Selected events

This section brings to the fore two different situations: a daily event showing the evolution of the frontal structures during three consecutive days in October 2008 (4.2.1) and a comparison between seasonal events; summer v/s spring 2012 (4.2.2) and winter v/s autumn 2009 (4.2.3) in order to examine the behavior of the submesoscale features under different climatic conditions. These particular years were chosen based on the availability of clear satellite images.

4.2.1 Daily events (October 2008)

When analysing the 10-year dataset (2003-2013), a limited number of consecutive cloud-free images (not more than three images) were retrieved. Some interesting situations - 24th, 25th June 2010 and 5th, 6th, 7th June 2006 (**see in Appendix C**), similar to October 2008, were investigated illustrating abrupt changes in frontal structures within an interval of a day. Therefore, to facilitate the readability of this chapter, only a particular event has been displayed below.

4.2.1.1 Chlorophyll-a concentration and Singularity exponents

In October 9th 2008, as observed from the satellite image of chlorophyll-*a* concentration, instabilities appear as meanders in the front (Figure 4.2 (a)) which successively spawn filaments. However, on the following day (Figure 4.2 (b)), the filaments seem to disappear but are again set into motion on the 11th (Figure 4.2 (c)). The images of the singularity exponents (Figure 4.2 right) show that the frontal structures are visible throughout the whole domain and they are almost similar for the three consecutive days.

(a)

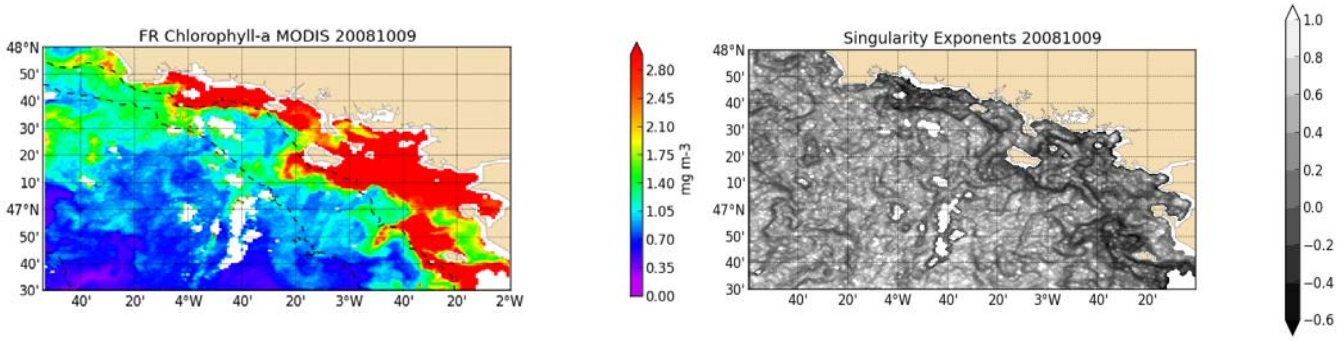

(b)

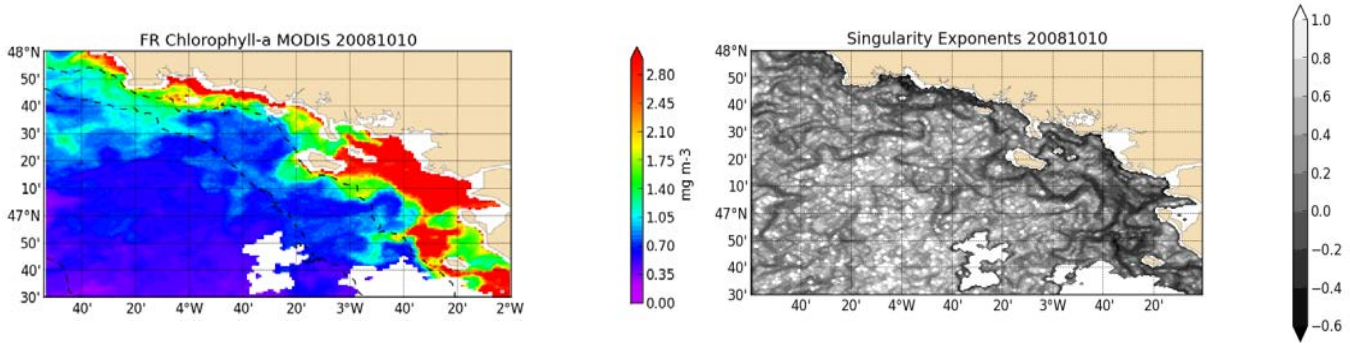

(c)

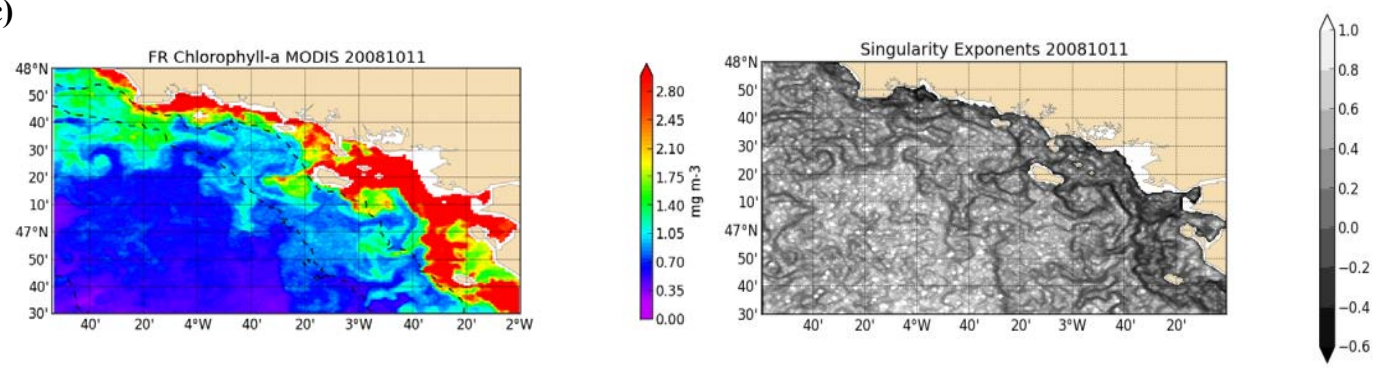

Fig 4. 2 Satellite images of Chlorophyll-*a* concentration (left) and corresponding singularity exponents (right) for three consecutive days in October 2008 (a - 09/10/2008, b - 10/10/2008, c - 11/10/2008)

4.2.1.2 Sea Surface Temperature (SST)

Satellite images of Sea Surface Temperature were analyzed for the same event to see whether there were any distinct differences compared to chlorophyll-*a* concentration. Figure 4.3 (a) shows the presence of cold water extending northwards and spreading with greater proximity to the coast. However, on the following day, the temperature increases throughout the whole domain and again decreases slightly on the 11th. From the analyzed observations, SST was found be of the order of a day. A clear evolution of the frontal structure is observed but it is not possible to visually estimate if their scale and intensity is changing during the considered period.

(a)

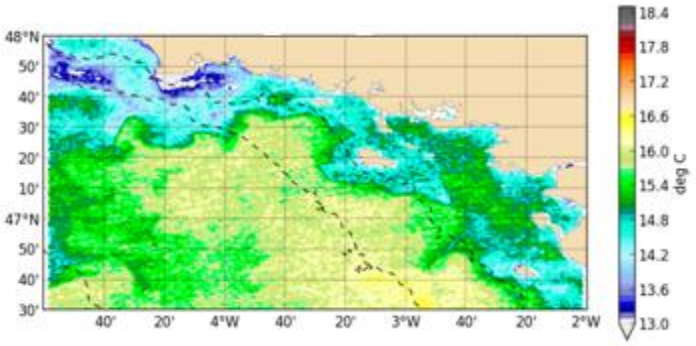

(b)

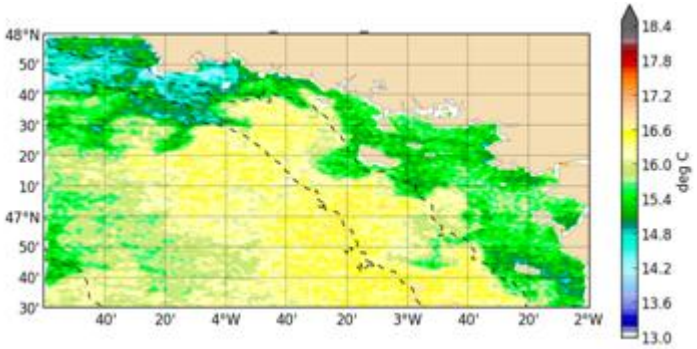

(c)

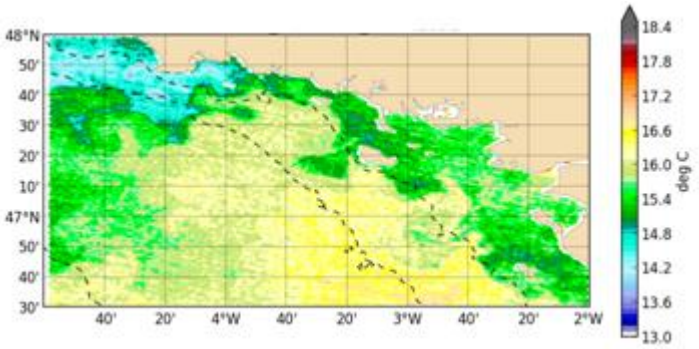

Fig 4. 3 Satellite images of SST for three consecutive days (a - 9th, b - 10th and c - 11th respectively).

4.2.1.3 Winds

In order to explain the decrease in filaments and the sudden increase in temperature on the 10th of October, the influence of the winds has been investigated. When analyzing the wind directions and strengths for a couple of days, it has been observed that on the 6th, 7th, and 8th of October (Figure 4.4), there were strong south-westerly or westerly winds. However, on the 9th and 10th, the wind reversed direction and decreased in intensity. An anticyclonic condition was also found to develop between northern Brittany and the English Channel on the 9th. Finally, the magnitude of the winds was found to increase again on the 11th in southern Brittany.

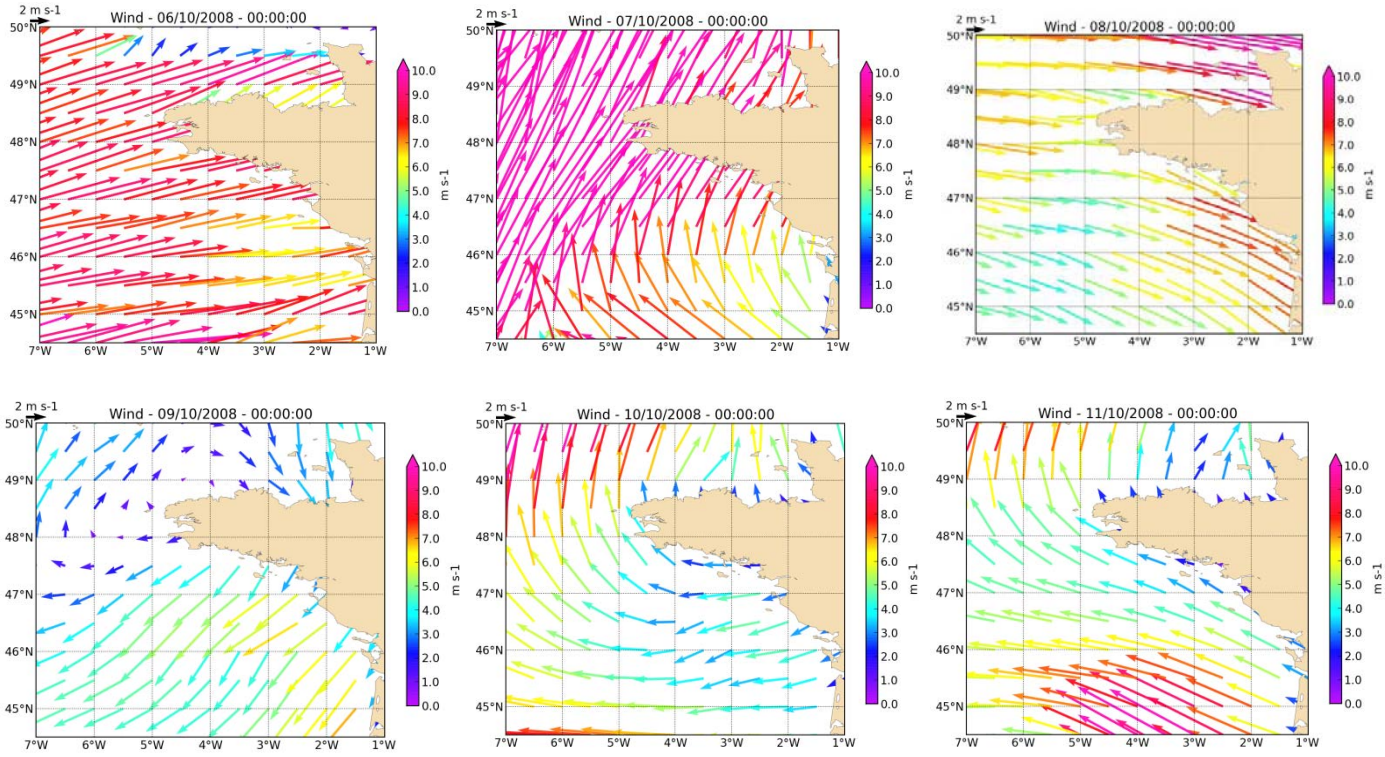

Fig 4. 4 Wind strength and direction from 6th to 11th October 2008

4.2.1.4 River runoffs

Since it is apparent that the winds have an influence on the frontal structures, the rate of river runoffs was also investigated to observe whether they contribute to this change in submesoscale features. Freshwater outflow rates were analyzed for both rivers Loire and Vilaine as they are adjacent and debouch into the southern part of Brittany (Figure 4.5). It was recorded that the rate of river runoff for the Vilaine is insignificant compared to the Loire being about 200 times higher compared to the former. During this period of the year, the rate of river runoffs is quite low and as observed in Figure 4.5 (left), the rate of river discharge remains unchanged on the 9th, 10th, 11th with an average outflow rate of about 250 m^3s^{-1}. It can also be noted that the minimum value is about 200 m^3s^{-1} during the first few days in August and attains up to 600 m^3s^{-1} by the end of the month.

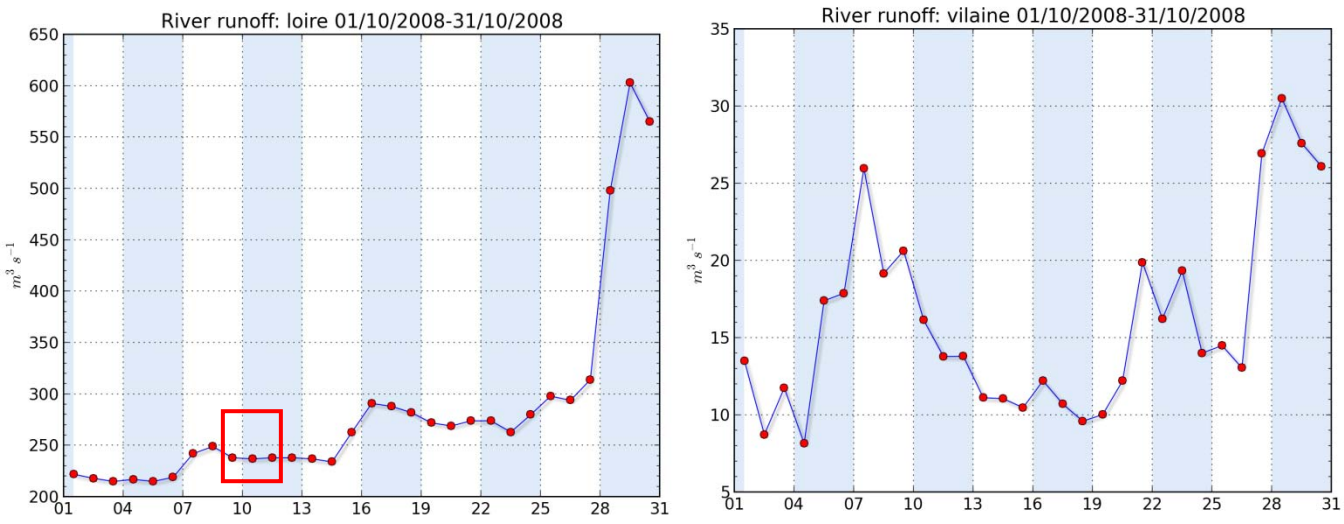

Fig 4. 5 Monthly flow rate data for Loire and Vilaine rivers in October 2008

After describing the chlorophyll-*a* concentrations, SPM, SST and impacts of the river runoff and winds for the selected event, some methods were put forward to characterize the submesoscale structures.

4.2.1.5 Fourier analysis

Figure 4.6 shows the power spectrum for the three consecutive days. This curve is plotted based on the singularity images for 9th, 10th and 11th October 2008. For these spatial scales analyzed, it is noticed that there is no significant peak highlighting a larger energy for a given scale. Furthermore, the spectra look very similar for the three dates. A line of best-fit was drawn for wavelengths ranging between 2.5 and 20 km to calculate the spectral slope for the 3 days, since wavelengths smaller than 2.5 km were considered as noise represented as wavy oscillations in Figure 4.6.

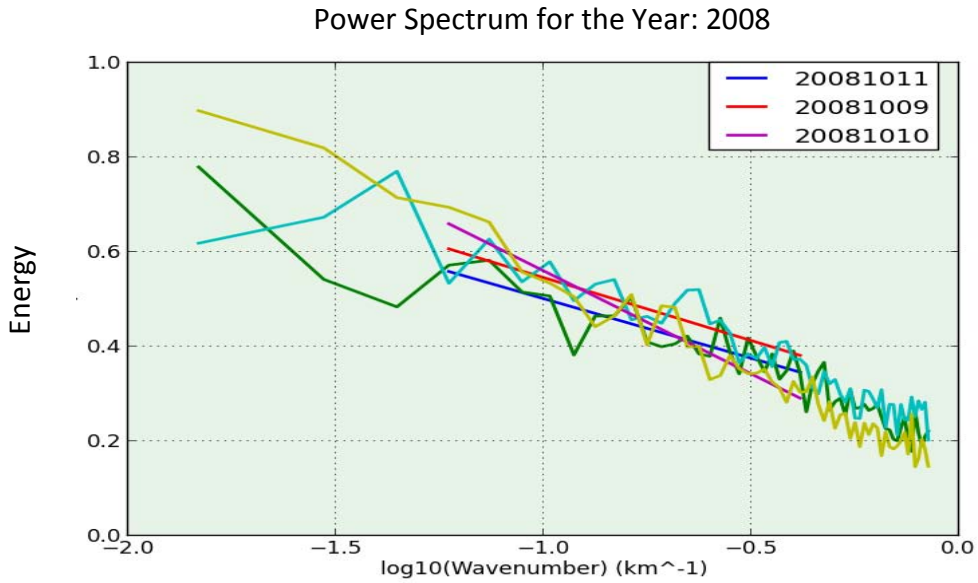

Fig 4. 6 Spectral analysis performed on the singularity exponent as a function of wave number. The 3 curves correspond to spectra for the 3 consecutive days, 9th, 10th and 11th Oct 2008. The straight lines are the slopes of the spectrum for the different dates.

The values of the spectral slopes are displayed in the Table 1 and they are found to lie within the same range. A slightly higher value is recorded on the 10th which is explained by the presence of clouds shown in Figure 4.2 (b).

Table 1 Values of Spectral slopes calculated for 9th, 10th and 11th October 2008.

DAYS	SPECTRAL SLOPE
9/10/2008	-0.266
10/10/2008	-0.436
11/10/2008	-0.252

4.2.1.6 Probability density function

The probability density curves (Figure 4.7) highlight a Gaussian distribution of the singularity exponents with a maximum number of occurrences, (mean) close to 0.2. However, the discrete distribution of the singularities is not symmetric: the tail on the right of the curve is longer compared to the left side for the three days meaning that they are positively skewed.

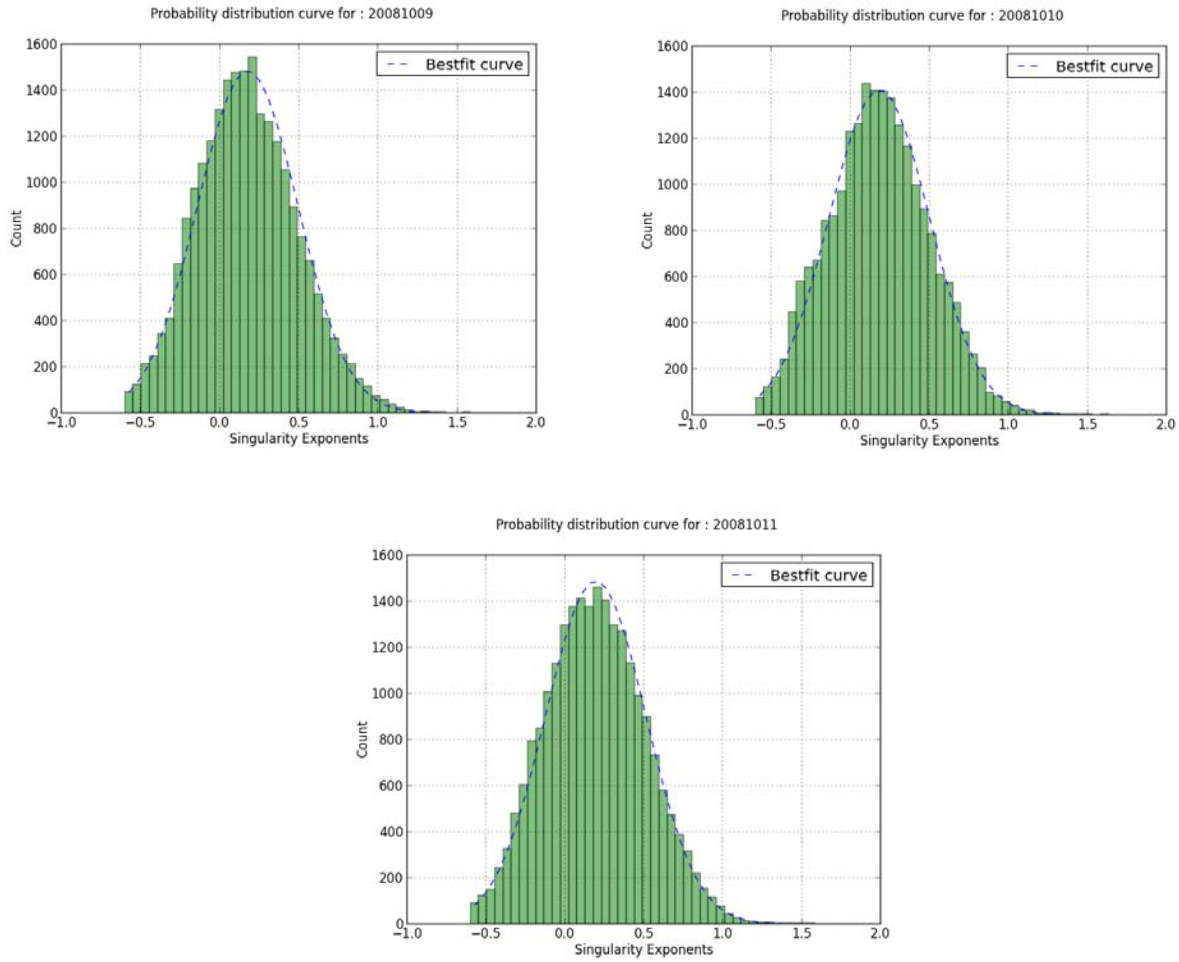

Fig 4. 7 Probability density curve performed on the singularity exponents for 9th, 10th and 11th respectively. Blue dashed line represents the best-fit curve.

The skewness values for the 3 days were calculated and represented in Table 2. They are all skewed-right implying that there is more density of occurrences in the lower part of the variable range (i.e. negative singularity exponents) as compared to the higher part of the distribution and that the mean is on the right of the peak value. It is observed that on the 10th of October, the

skewness value is lower compared to the other days and it is interesting to note that it coincides with the decrease in chlorophyll-*a* concentration.

Table 2 Skewness computed for the three consecutive days

	SKEWNESS
9/10/2008	0.264 (Right)
10/10/2008	0.160 (Right)
11/10/2008	0.177 (Right)

4.2.2 Comparison between spring and summer 2012

After analyzing the daily evolution of the submesoscale structures, another approach was put forward to identify marked differences between the seasons and understand the processes involved during these periods. Spring and summer were compared because the structures of the phytoplankton biomass showed two contrasted events as viewed from the ocean color images. Analyzing summer and spring periods for a 10-year dataset have shown that all the years appear similar in terms of structures. Consequently, the reason for choosing 2012 is that the images during summer for this particular year were free from clouds resulting in better analysis.

4.2.2.1 Chlorophyll-a concentration and singularity exponents

As observed from the satellite imagery (Figure 4.8 top left), chlorophyll-*a* is concentrated on both the coastal area and the outer shelf. These marked phytoplankton blooms represented as multi-colored swirls in the water, begin to emerge by the end of March and die down by May. This bloom appeared primarily in stratified and clear waters at the boundary of the oceanic water and plumes of southern Brittany Rivers (mainly the Loire and Vilaine). Comparing to the oligotrophic condition in summer, it can be deduced that the plumes are much confined alongshore. The difference between the singularity exponents for the 2 seasons clearly shows that the frontal structures are far more intense in spring (with larger negative singularity exponents) than in summer.

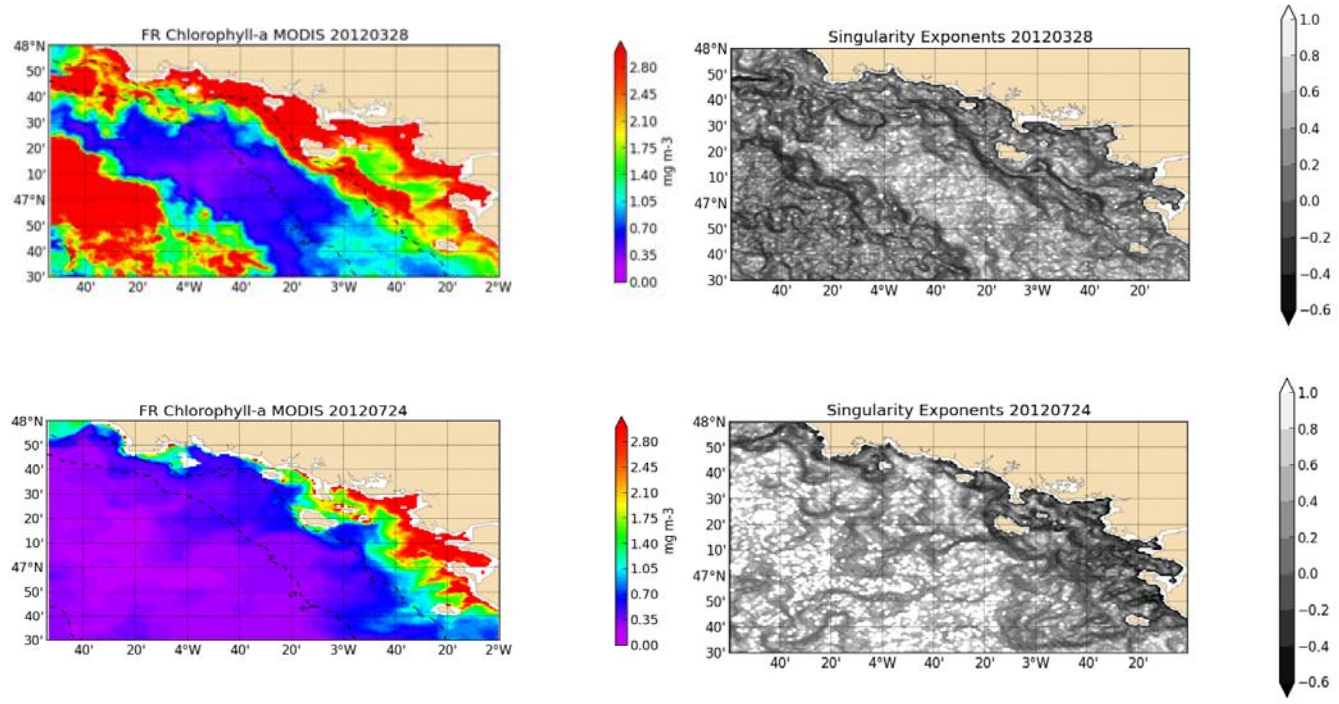

Fig 4. 8 Satellite imagery of chlorophyll-*a* concentration (left) and corresponding Singularity exponents (right) for spring – 28th March 2012 - (top) and summer – 24th July 2012 - (bottom) 2012.

4.2.2.2 Sea surface temperature and Suspended particulate matters

The SST color bar (Figure 4.9 left) clearly shows that the temperature in summer is higher than in spring. The SST in March (Figure 4.9 top left) reproduces the same spatial patterns as the chlorophyll-*a* image in Figure 4.8. A cold water mass in summer is found to develop between longitude -3°40'W to -5°W. A satellite image of SPM (Figure 4.9 top right) in spring exhibits a marked degree of patchiness dispersed offshore being coherent with the chlorophyll-*a* concentration image in Figure 4.8. In contrast, the river plume is confined near shore during summer.

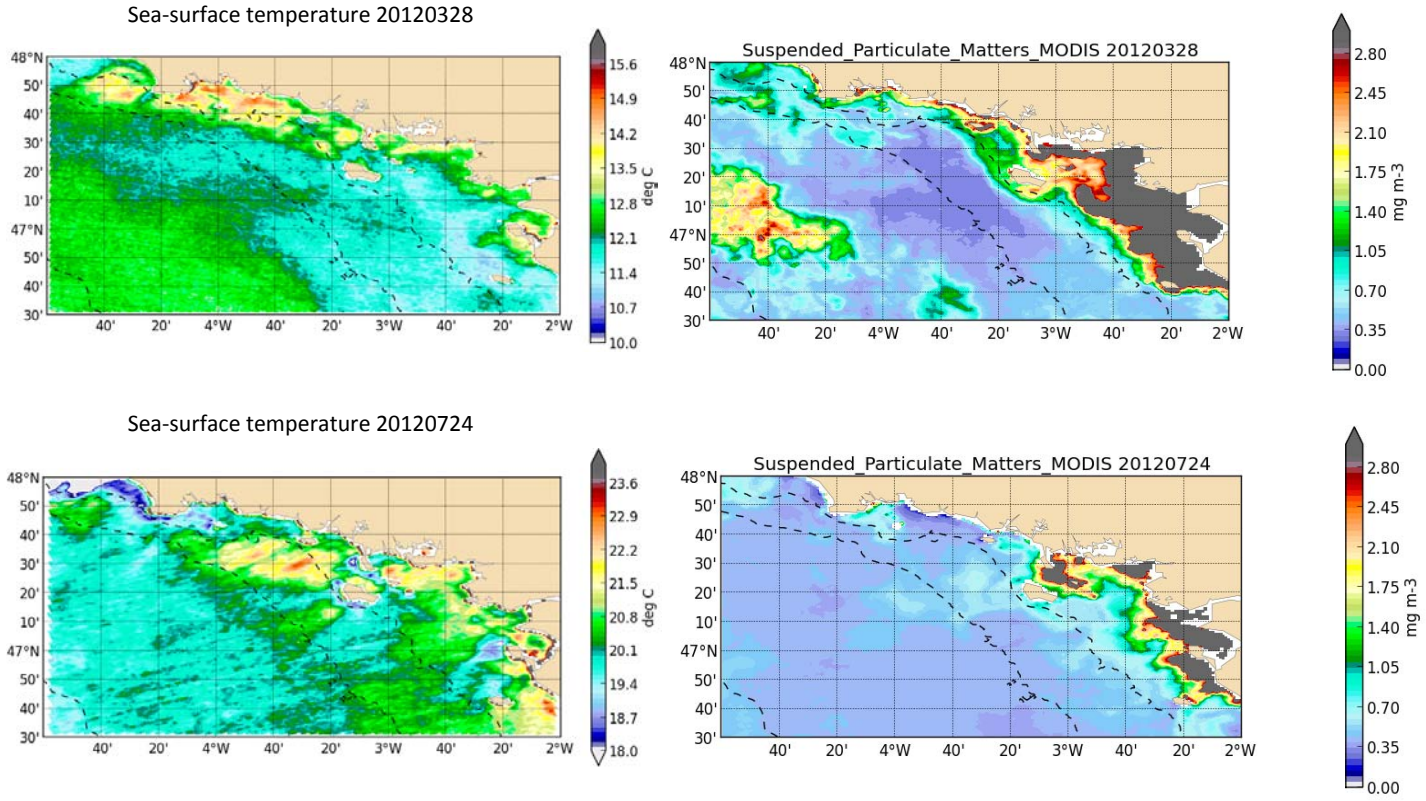

Fig 4. 9 Sea surface temperature (left) and suspended particulate matters (right) observed during spring – 28th March 2012 - (top) and summer – 24th July 2012 - (bottom)

4.2.2.3 Winds

From the 26th to 28th March (Figure 4.10), there was a steady and dominant north-easterly wind blowing with an average speed of about 7 m s^{-1}. However, between 22nd and 24th July, the intensity of the wind decreases to about 4 m s^{-1} but the direction of the wind remains the same. In this example, two contrasted seasons with similar wind conditions and clear sky conditions were obtained.

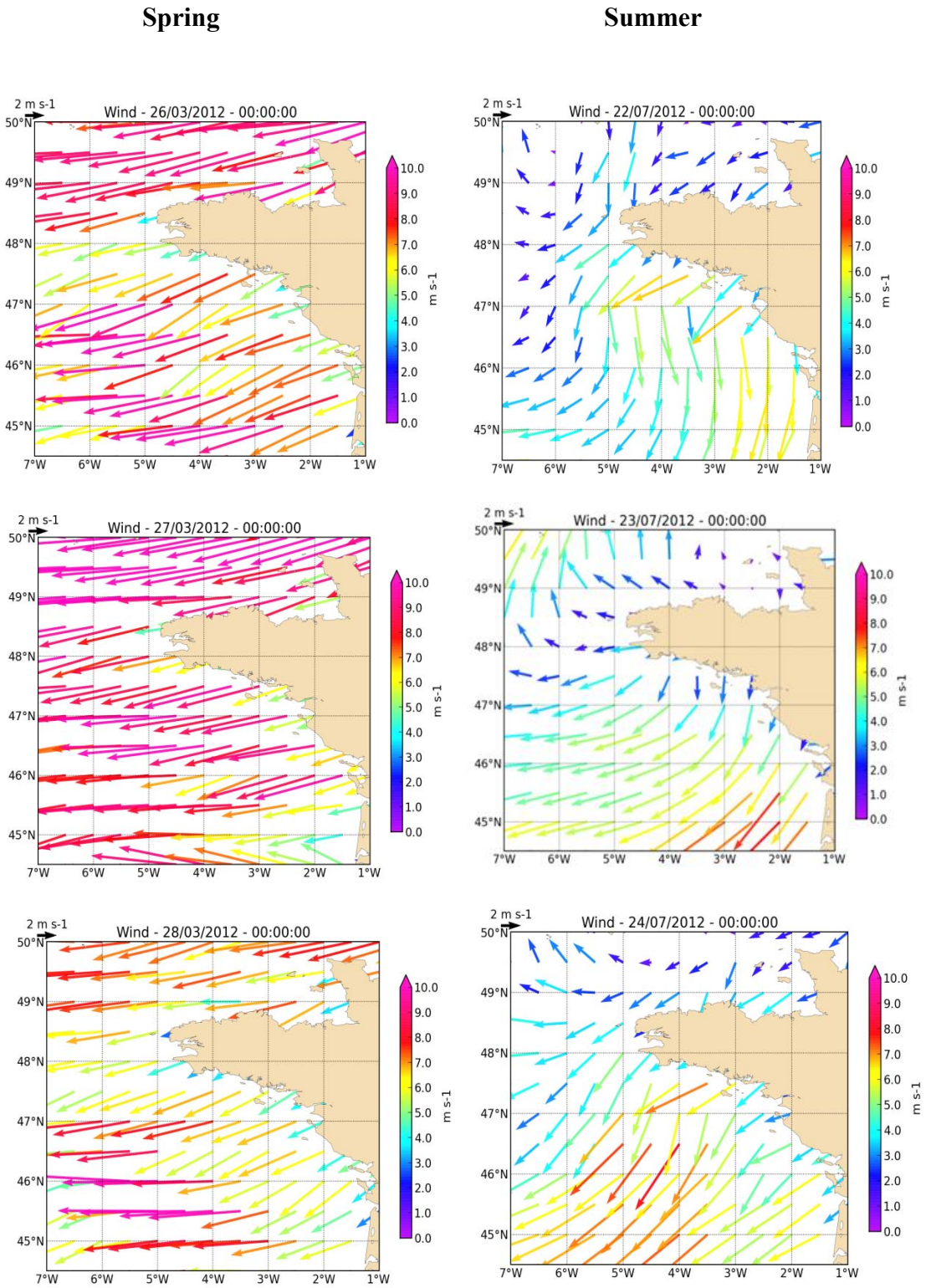

Fig 4. 10 Winds strength and direction for spring (26th to 28th March 2012 - left) and summer (22nd to 24th July 2012 - right) 2012.

4.2.2.3 River runoffs

The rate of freshwater discharge for the Loire River was also analyzed and compared for both seasons. On the 28th March, a flow rate of about 425 m^3s^{-1} was recorded being higher compared to 275 m^3s^{-1} recorded on the 24th July (Figure 4.11).

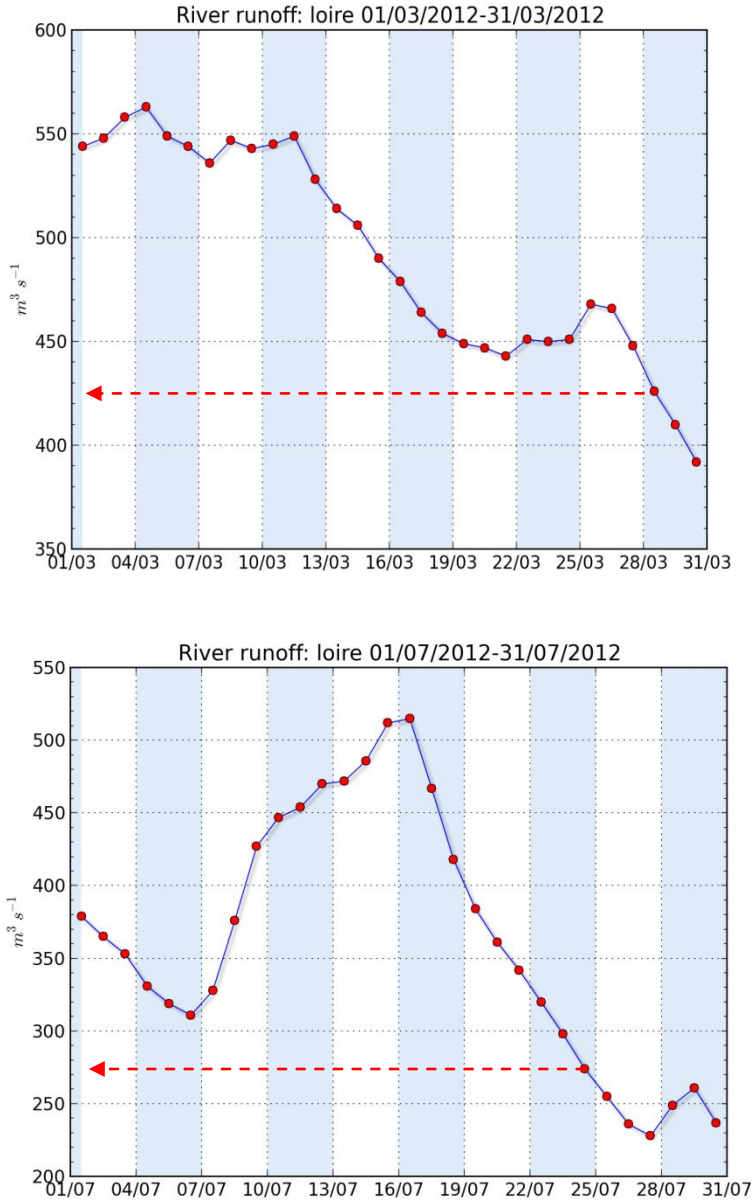

Fig 4. 11 Daily river runoffs data measured at Sainte-luce Station (Loire River) for March (Top) and July (Bottom) 2012.

4.2.2.5 Fourier analysis

A Fourier transform was performed on the two selected dates to represent each season (Figure 4.12). As observed from both curves, the spectra look very similar with no significant peaks detected for wavelengths between 2.5 km and 20 km. This therefore indicates that no dominant energy value is detected at any spatial scale.

Fig 4. 12 Fourier transform performed on 28th March 2012 in spring and 24th July 2012 in summer 2012. Spectral slopes calculated for wavelengths between 2.5 and 20 km. Wavelengths less than 2.5 km are considered as noise.

The spectral slopes for 28th March and 24th July were calculated for wavelengths ranging between 2.5 and 20 km and the values are represented in Table 3. Although the submesoscale structures showed marked differences in the chlorophyll-*a* images, the values of the spectral slopes are similar.

Table 3 Values of spectral slope calculated for the two selected dates in spring and summer 2012.

Dates	Spectral Slope
28/03/2012	-0.353
24/07/2012	-0.325

4.2.2.6 Probability density function

The probability density function was plotted for 28th March and 24th July 2012. Figure 4.13 clearly shows that the curve is skewed-right (right tail longer than left tail) during spring and skewed-left during summer. It is therefore deduced that the intensity of the frontal structures is higher in spring in comparison to summer.

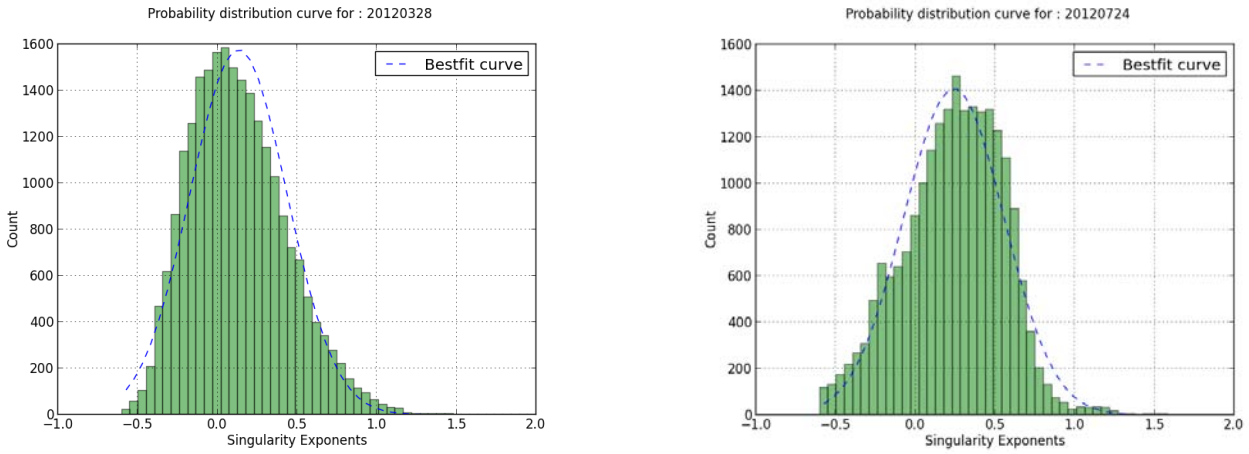

Fig 4. 13 Probability density curve plotted for 28th March (Left) and 24th July 2012 (Right). Blue dashed curve represents the best fit curve.

When calculating the skewness values (Table 4) for 28th March and 24th July 2012, it is noted that the values agree with the PDF curves (skewed-right in spring and skewed-left in summer).

Table 4 Values of skewness computed for the 28th March 2012 and 24th July 2012.

	Skewness
28/03/2012	0.514 (Right)
24/07/2012	-0.184 (Left)

4.2.3 Comparison between autumn and winter 2009

After analyzing spring and summer, the next objective was to compare the two other seasons; winter and autumn. When investigating the whole dataset (2003-2013), similar winter and autumn structures were identified for all the years, but due to unavailability of cloud-free images during these periods, the year 2009 (showing less cloud pixels), was chosen to better illustrate and monitor the submesoscale processes.

4.2.3.1 Chlorophyll-a concentration and Singularity exponents

The river plumes in winter (Figure 4.14 top left) generally show fewer frontal structures at small scales which extend further from the coast compared to autumn where they meander more and are less spread offshore. The striking difference in the singularity exponents images is the strong gradient visible in February (Figure 4.14 top right), indicating intense frontal activities about 150 km from the coast compared to autumn (Figure 4.14 bottom right), where the intensity of the fronts are strong and uniform throughout the whole domain.

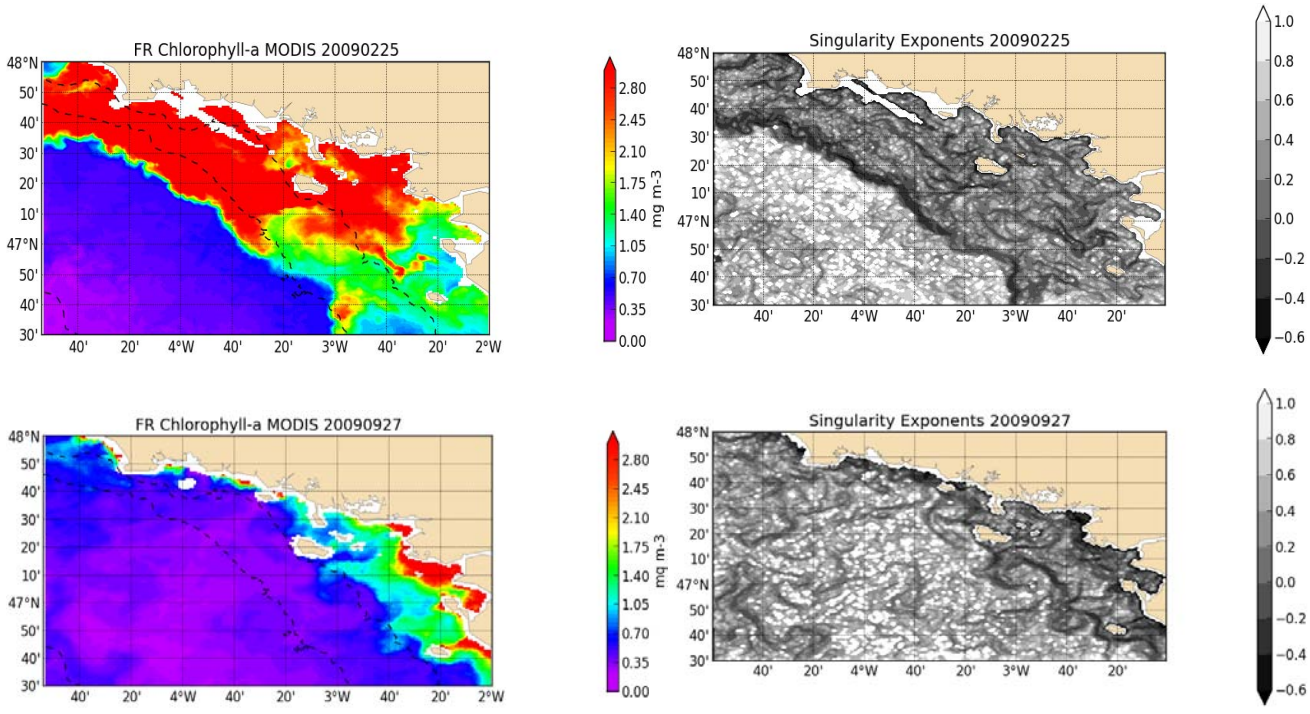

Fig 4. 14 Chlorophyll-a concentration (left) and corresponding singularity exponents (right) for 25th February 2009 (top) and 27th September 2009 (bottom).

4.2.3.2 Sea Surface Temperature and Suspended Particulate Matters

The SPM image in winter (Figure 4.15 top left) shows how far the river plumes extend offshore compared to autumn (Figure 4.15 bottom left). From the remotely-sensed image of sea surface temperature, a cold cross-shore gradient close to the coast is observed in winter (Figure 4.15 top right) with warmer water extending offshore. The SST in autumn (Figure 4.15 bottom right) appears to be warmer by 10 degrees in contrast to winter as indicated on the color bar. Similar to chlorophyll-*a* images (Figure 4.15 left), the SST images show differences in submesoscale structures; fewer frontal features during winter and more meanders in autumn.

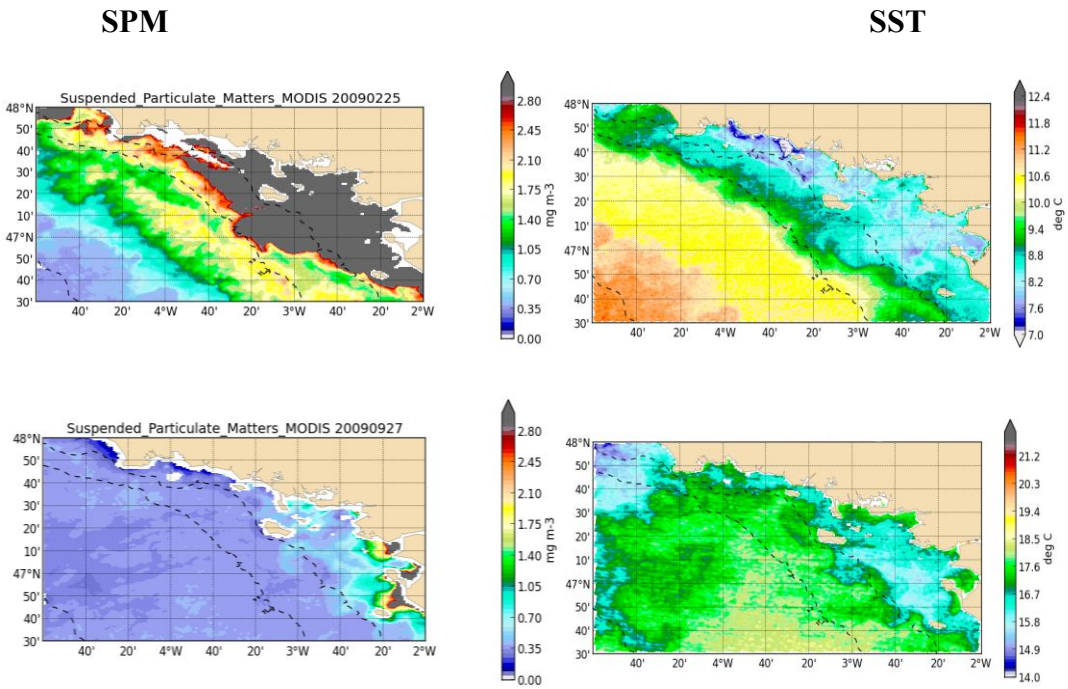

Fig 4. 15 Comparing Suspended particulate matters for winter (25th February) (top left) v/s autumn (27th September) (bottom left) and Sea Surface Temperature for winter (top right) v/s autumn (bottom right).

4.2.3.3 River Runoffs

Analyzing the rate of river runoffs will help to explain why the SPM and Chlorophyll-*a* concentration images in winter are extended offshore compared to autumn where, the river plumes are constrained alongshore. Figure 4.16 (top) shows that the rate of river runoffs measured in winter was about 1000 m^3s^{-1} which is 10 times higher than in September (Figure 4.16 bottom).

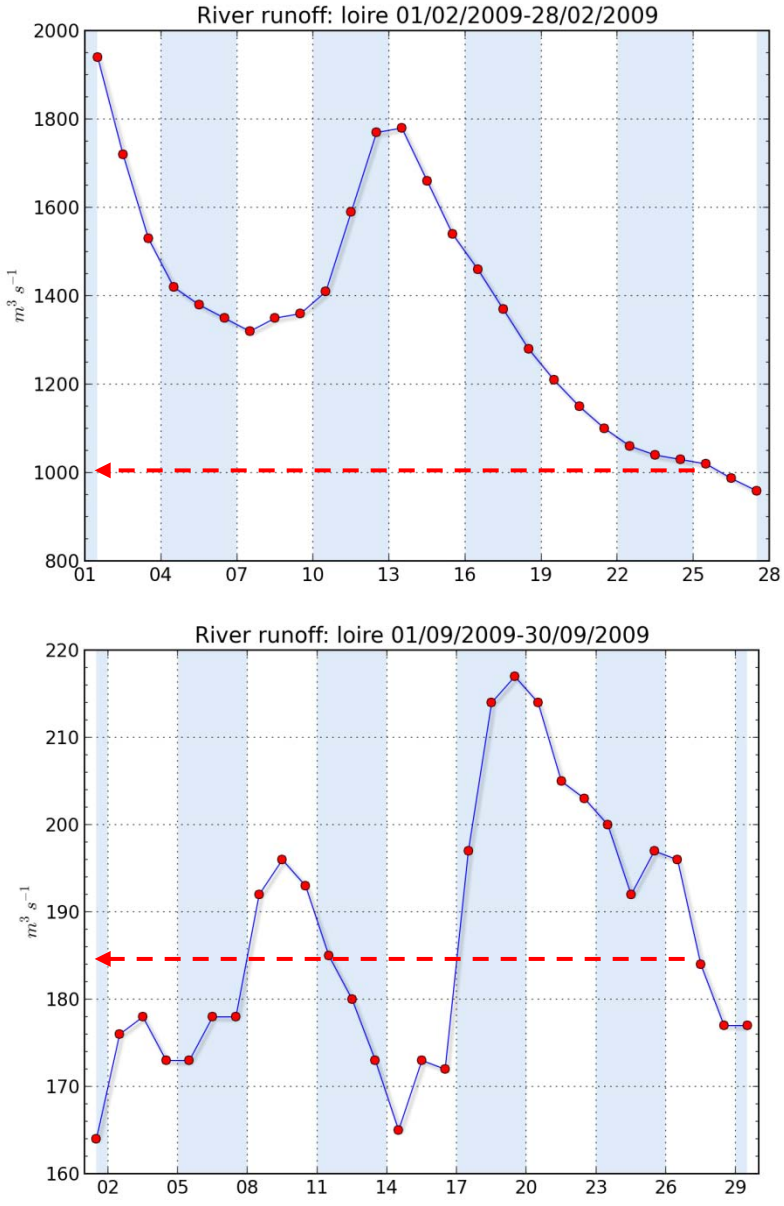

Fig 4. 16 Rate of river runoffs for the months of February and September 2009.

4.2.3.4 Winds

After analyzing the rate of river runoffs, the magnitude of the winds was also investigated in order to see whether it has an impact on the river plumes. As observed from Figure 4.17, the intensity of the winds in winter is higher than that in autumn. However, similar wind direction was noted during winter and autumn (wind maps not shown).

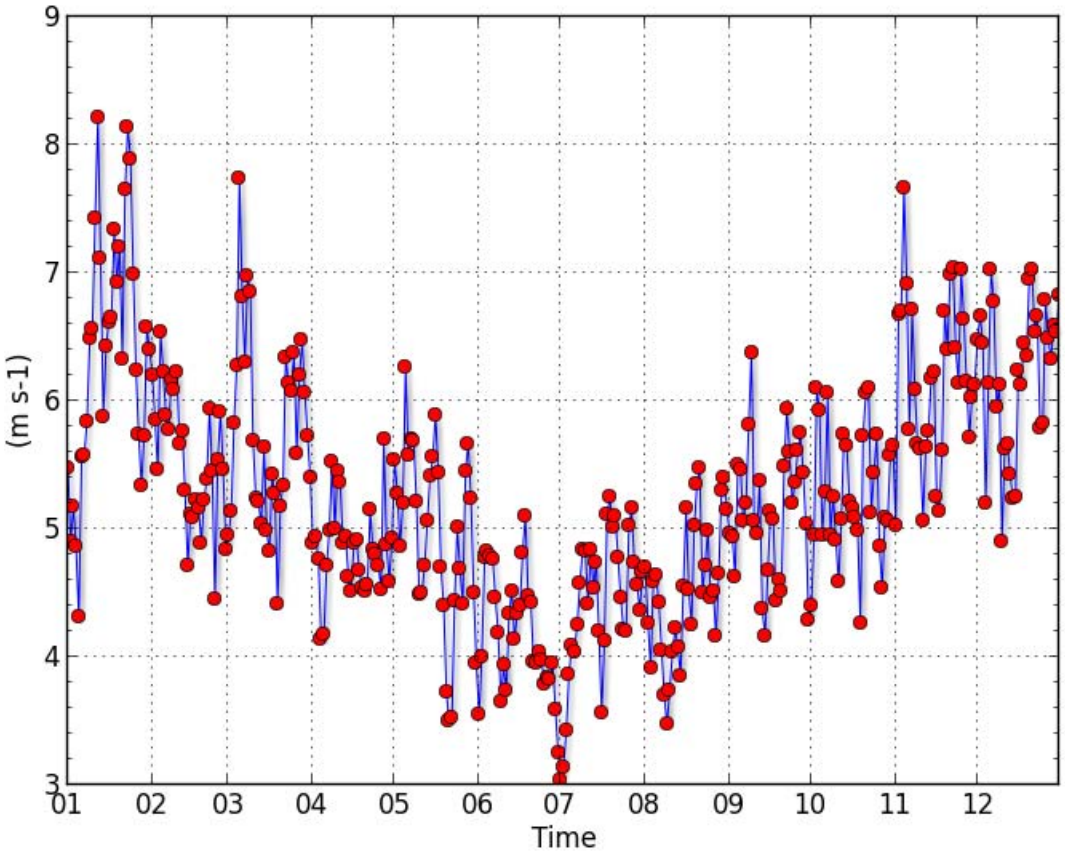

Fig 4. 17 Wind intensity averaged over the domain measured for year 2009.

4.2.3.5 Fourier analysis

A Fourier transform was performed on the 27th September and 25th February 2009 to represent each season; autumn and winter respectively (Figure 4.18). As observed from both curves, the spectra look very similar with no significant peaks detected for wavelengths between 2.5 km and 20 km. This therefore indicates that no dominant energy value is observed at any spatial scales.

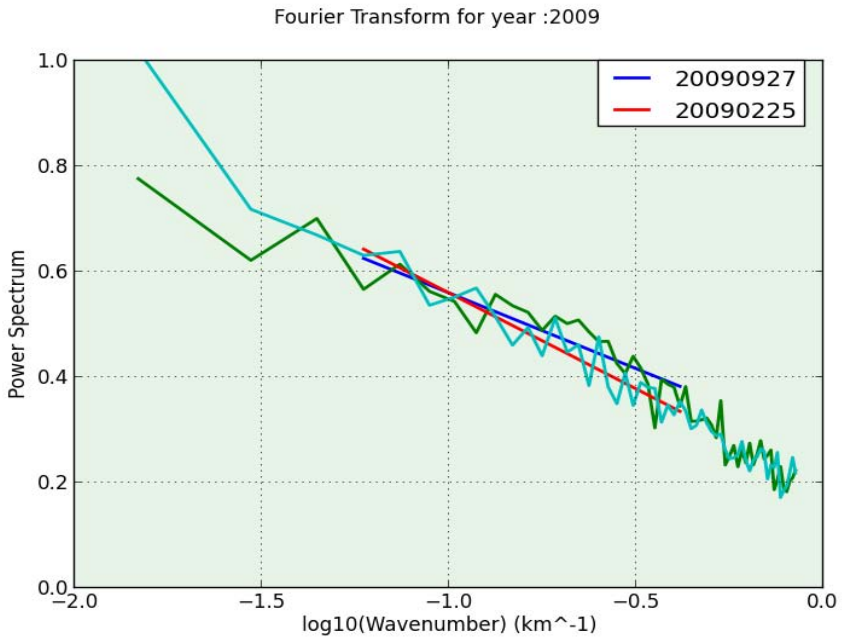

Fig 4. 18 Fourier transform performed on 25th February and 27th September 2009.

The spectral slopes for 25th February and 27th September were calculated and their values are represented in Table 5. Although the submesoscale structures showed distinct contrasts on the chlorophyll-*a* concentration images, the values of the spectral slopes display no significant differences.

Table 5 Values of spectral slopes recorded for 25th February and 27th September 2009

	Spectral slope
25th February 2009	-0.364
27th September 2009	-0.287

4.2.3.6 Probability density function

After analyzing the spectral slopes, the probability distribution curves were examined on the 25th February and 27th September 2009 (Figure 4.19). Both dates highlight a Gaussian distribution of the singularity exponents with a maximum number of occurrences close to 0.2. The differences between the two seasons lie in the shape of their distribution, where in winter the graph shows a wider distribution in contrast to autumn.

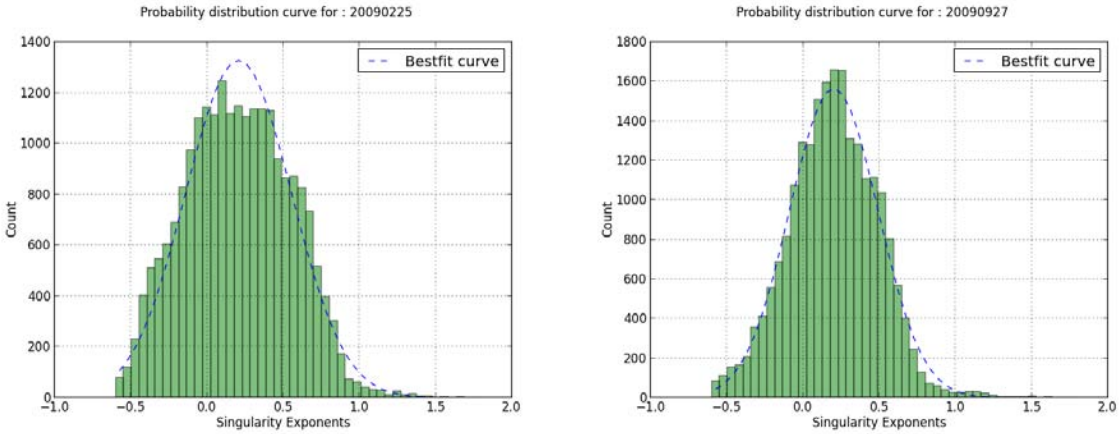

Fig 4. 19 Probability density function plotted for 2 selected dates in winter and autumn 2008

The skewness values for both dates were calculated and represented in Table 6. They are both skewed-right implying that each season shows strong frontal activities. However, a slightly higher skewness value was noted in winter compared to autumn.

Table 6 Values of skewness computed from the probability density function for 2 selected dates in winter and autumn 2009.

	Skewness
25th February 2009	0.124 (Right)
27th September 2009	0.076 (Right)

4.3 Interannual Variability

After analyzing some events on a daily and seasonal scale, a period of 10 years (2003-2013) was investigated in order to describe the interannual variability from the hydrodynamic parameters below and whether they correlate with each other with a view to understanding the different processes involved.

4.3.1 River runoffs

The rate of river runoffs was plotted from a 10-year dataset (2003-2013) (Figure 4.20). A seasonal cycle is observed; higher outflow rate in winter compared to summer. There are some years for which the highest rate of river runoffs recorded in winter is reaching 3000 m^3s^{-1}; namely 2003, 2004, 2006, 2007 and 2013. Summer 2007 and 2008 have the highest rate of river runoffs compared to the other years. This figure highlights the strong interannual variability of the river runoffs related to the weather conditions. The year 2008 is noteworthy with large river discharge throughout the whole year.

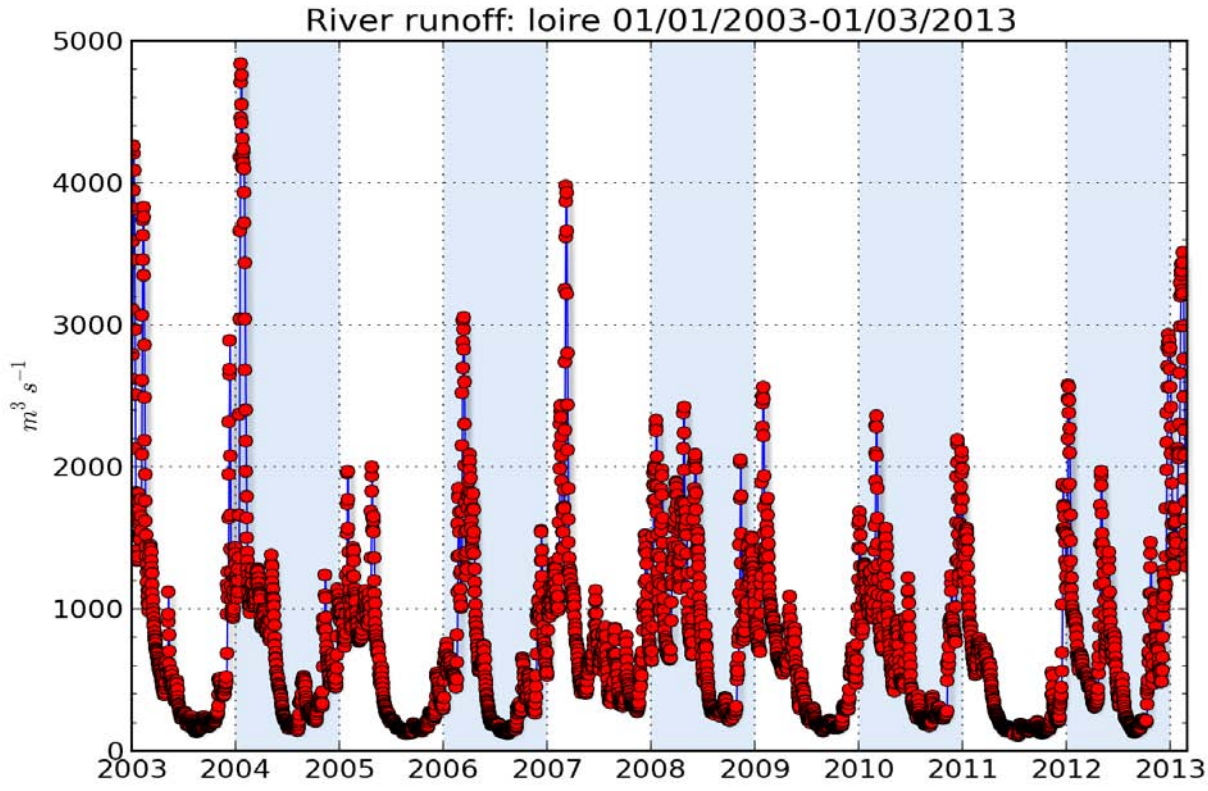

Fig 4. 20 Daily river runoffs computed for a period of 10 years

4.3.2 Mean Chlorophyll-a concentration

The mean of chlorophyll-*a* concentration, computed over the domain, was also plotted for the whole time series January 2003 to June 2013. Figure 4.21 shows a seasonal cycle with higher peaks corresponding to higher mean chlorophyll-*a* in spring and a small averaged production in summer. Higher peaks were observed in 2004, 2006, 2007, 2008 and 2012.

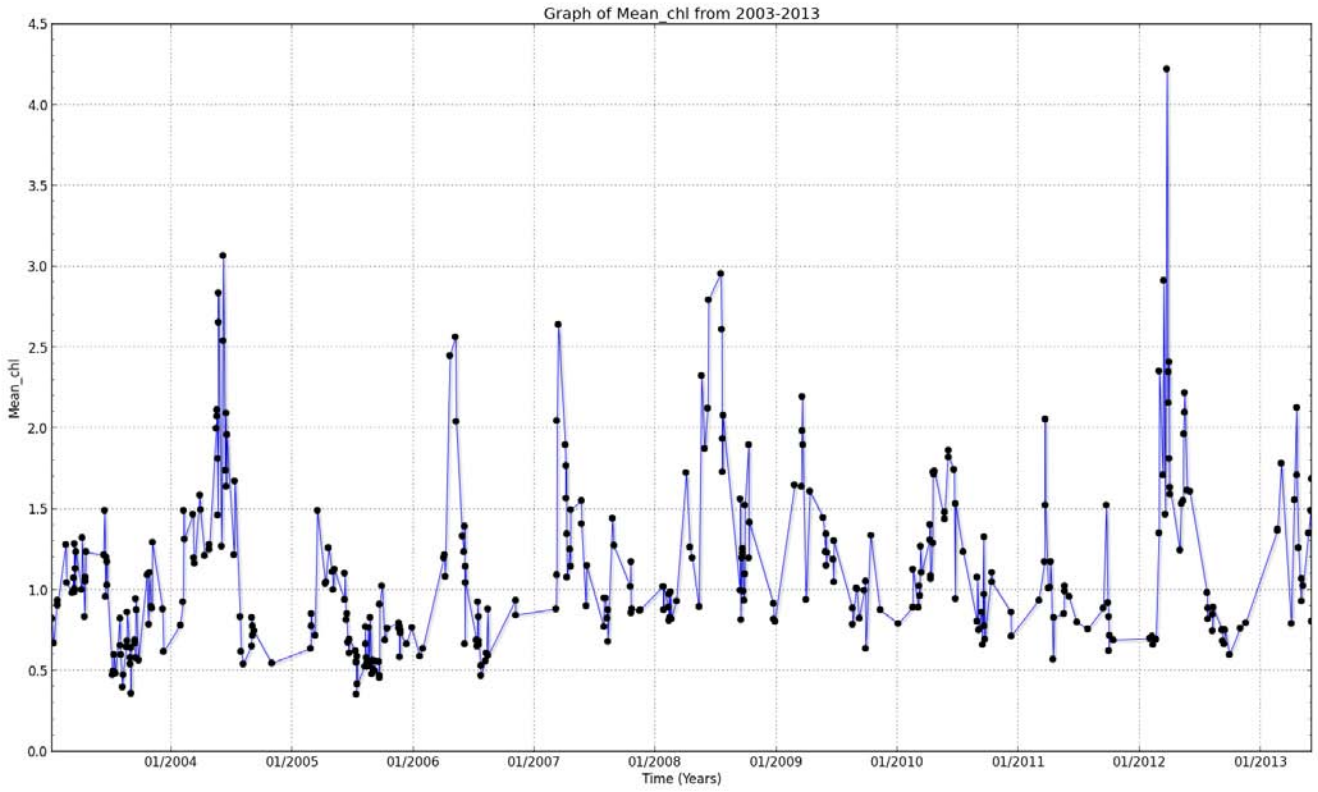

Fig 4. 21 Graph of mean chlorophyll-*a* concentration for cloud-free images plotted from 2003-2013.

4.3.3 Wind Intensity

The wind intensity was plotted from January 2006 to June 2013 (the period is shorter than periods for other parameters due to atmospheric model availability) and it shows a distinct seasonal pattern (Figure 4.22). Higher wind intensity of about 7.5 m s^{-1} is observed during winter compared to 3.5 m s^{-1} in summer.

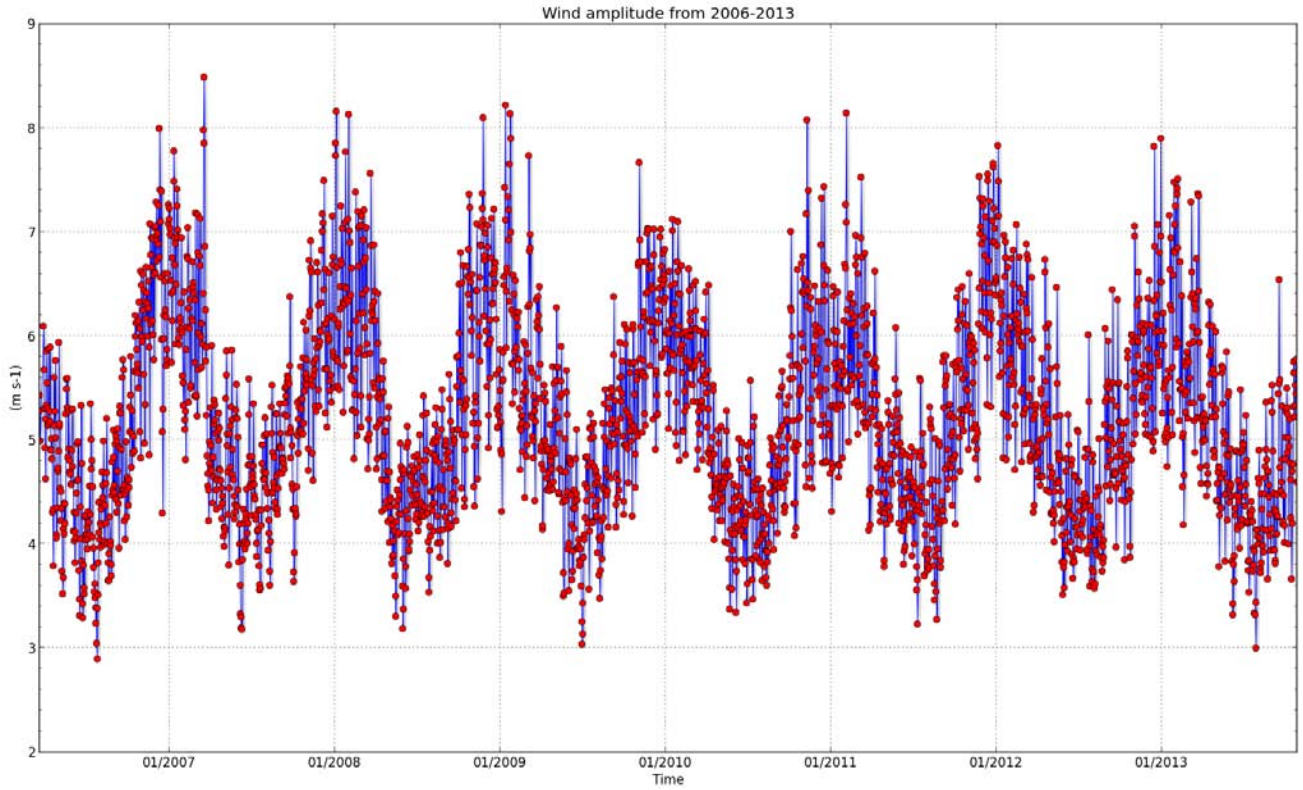

Fig 4. 22 Averaged wind intensity over the domain from January 2006 to June 2013

4.3.4 Skewness

To characterize the frontal activity, the skewness values performed from singularity exponent distributions, were plotted on a 10-year dataset for cloud-free images only. Figure 4.23 indicates if there is any seasonal cycle and in turn, it can also estimate whether the graph correlates with the rate of river runoffs or wind intensity. On this plot, a seasonal cycle is observed; positive or larger skewness value (Skewed-right) during periods of high runoffs/winter and negative skewness (left-skewed) during summer. This means that stronger frontal activities are more prevalent in winter than in summer.

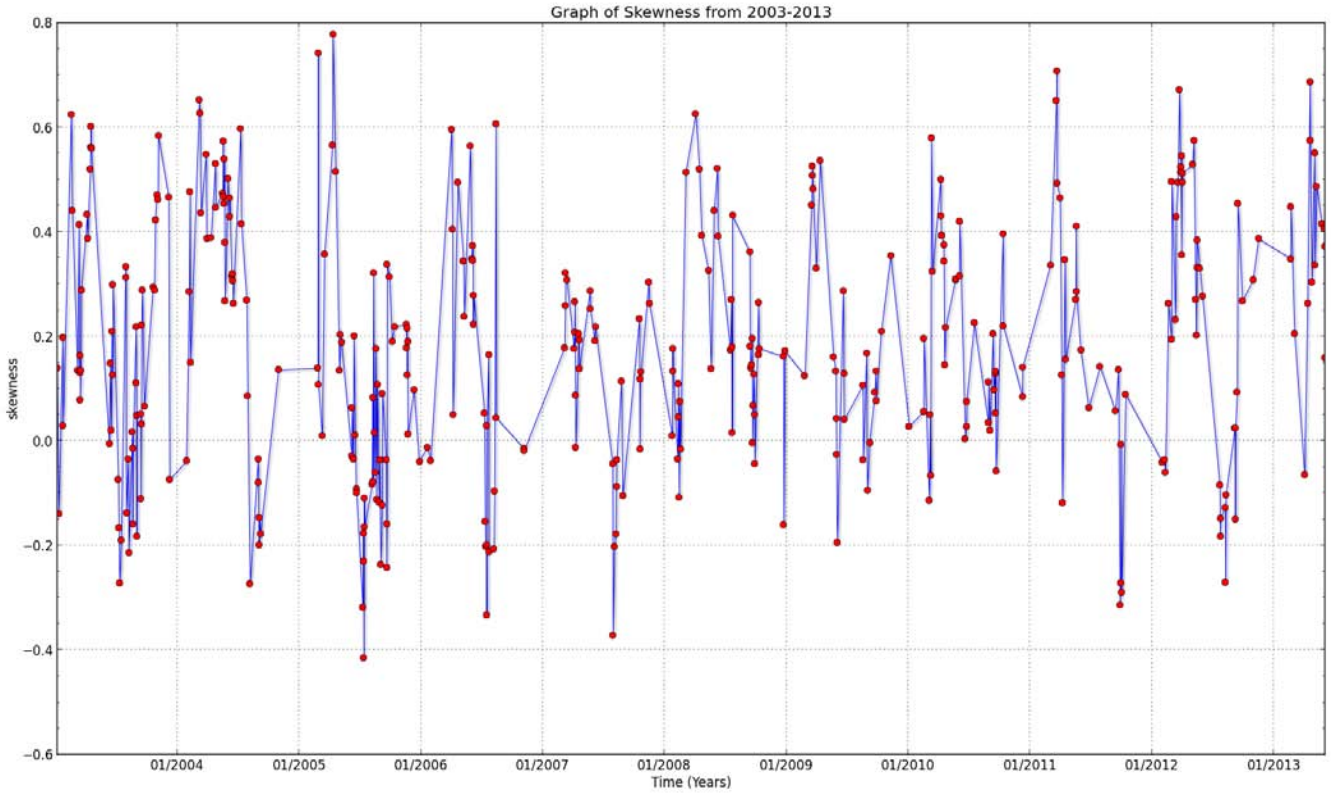

Fig 4. 23 Graph of skewness values for cloud-free images only plotted from 2003-2013

Several events on a daily, seasonal and interannual scale are investigated and compared throughout this chapter. The spectral slopes are also plotted on a 10-year dataset (2003-2013) (see appendix D) but no apparent seasonal variability is observed. However, the probability density function method is proved to be a reliable way to characterize submesoscale structures. Winds and river runoffs are analyzed and it is observed that they have indeed an impact on the evolution of the submesoscale structures, which will be further discussed in the next chapter. Furthermore, the singularity analysis is found to be an effective method to track frontal activities in the upper ocean.

Chapter 5 Discussion

The response of phytoplankton to submesoscale dynamics depends on the factor being the most influential over the phytoplankton growth. It can be nutrients carried away by freshwater discharge or upwelling or it can be controlled by the Photosynthetically Available Radiation. Since these components vary throughout the year, the first aim of this investigation is to analyze upper ocean tracers like chlorophyll-*a* concentration in the plume region off the Loire River and their possible relationships with the rate of river runoffs and winds. Thereafter, upon identifying the submesoscale features, they are then characterized by some statistical methods. Three time scales were considered:

(i) Daily

(ii) Seasonal

(iii) Inter annual variability

5.1 Daily Scale

Discussion on event in October 2008

This particularly event was selected because, based on the limited number of cloud-free images, direct observation of chlorophyll-*a* concentration for 3 consecutive days were very sparse. The evolution of the submesoscale fronts changes rapidly with a temporal variability of the order of a day (*Lévy et al., 2012 and Capet et al., 2008a*) and this proves how energetic the submesoscale regime is (*Denman and Abbott, 1994)*. The maps of the singularity exponents plotted were used to determine whether there was any visible contrast in the frontal structures, but apparently the submesoscale features were ubiquitous (*Capet et al., 2008a*), even under persistent instabilities. The SST increase observed on the 10th of October (Figure 4.3) could result from the decrease in filaments and it is principally due to a wind relaxation occurring on that day (Figure 4.4). The common feature that normally appears during this period of the year known as the warm water tongue (*Koutsikopoulos and Le Cann, 1996)* which also contributes to the SST increase. Every time the wind slackens and the turbulence regime is reduced, the submesoscale features are expected to largely accelerate the surface restratification, thus changing the upper ocean tracer's dynamics or structures (*Capet et al., 2008a*). In fact other authors *(Puillat et al., 2004, Ferrer et al., 2009, Petus et al., 2010 as cited in Batifoulier et al.,2012)* have found that river plume

dynamics are commonly influenced by wind regimes. However, freshwater discharge does not seem to have an influence on the river plumes in this case, as the rate of river runoffs measured was practically unchanged during the 3 days (Figure 4.5 top).

The power spectrum of kinetic energy is used to characterize the energy distribution in terms of spatial scales *(Thomas et al., 2008).* A nearly flat horizontal spectral slope exhibits a characteristic -0.2 power law for 9th and 11th of October. However, a slightly steeper spectral slope (-0.4) was obtained on the 10th but the small part of the spectrum selected is not sufficient to confirm if this difference is significant (Figure 4.6). The other method applied to characterize submesoscale structures is the use of the probability density function in which the skewness determines the occurrence of intense fronts. Positive skewness obtained on the 3 days implies that strong fronts were present in October. However, the 2nd day shows a lower skewness value indicating a weaker frontal activity, which coincides with the decrease in submesoscale filaments.

5.2 Seasonal Variability

Spring and summer 2012

Patchiness of chlorophyll-*a* concentration from satellite images, represented as multi-coloured swirls (Figure 4.8 top left), are only visible during spring or late winter. These phytoplankton blooms are events of fast primary productivity generated from responses to driving forces in the ocean like upwelling, wind or river runoff. These blooms have different timescales; they can be frequent seasonal phenomena or momentary or intermittent events related to climatic conditions (*Cloern 1996, Cloern 2001, Cloern 2010*). The explosive primary productivity around March is triggered by a conjunction of suitable factors like warmer waters, more sunlight (*Bergeron and Koueta, 2011*) and nutrient enrichment carried by river outflows along the coast or upwelled deep water over the shelf break (*Pichon and Correard, 2006*). When the river discharge is reduced (Figure 4.11 top) and prevailing winds are from the north (upwelling-favourable) (Figure 4.10 left), the northward movement of the plumes is dispersed offshore and this type of event is usually present during spring (*Lazure et al., 2008).*

The decreasing extent of the river plume in summer is mainly due to low river flows (Figure 4.11 bottom) and weaker winds (Figure 4.10 right). According to *Lunven et al., 2005,* limited amounts of nutrients brought by river runoffs (Figure 4.9 bottom right) are taken up quickly by the phytoplankton. The increased solar irradiance in summer causes the water column to remain stratified from the end of June to beginning of September thus impeding primary production near the coast. Although different seasons were compared, both dates have more or less the same spectral slope of about -0.3. However the spectral value obtained does not coincide with those given in the literature *(Capet et al., 2008 and Klein et al., 2008),* but this is probably due to the fact that the region chosen for investigation and then the spatial scales considered were too limited. From the singularity exponent images, it can clearly be observed that the frontal structures are much stronger in spring compared to summer and this is confirmed from the PDF method, indicating positive skewness in March and negative skewness in July (Table 4). According to *Lévy et al., 2012*, strong fronts indicate intense submesoscale dynamics, which can control the movement of the phytoplankton. Consequently, an assumption could be that strong winds in spring account for a larger production and initiate more instabilities explaining this positive skewness.

Winter and autumn 2009

River plumes in winter usually have less meandering and extend northwards along the inner shelf (Figure 4.14 top). The extent of the river runoffs depends principally on the amount of freshwater discharge and also on the river outflow regime on a seasonal or annual basis *(Cravo et al., 2006, Signoret et al.,2006 as cited in Lihan et al., 2011).* As studied by *Lazure et al., 2004*, during the winter season, downwelling-favourable winds prevailing from the south-west tend to drag the density-driven plumes towards the North. Intense river runoffs (Figure 4.16 top) during this period alter the dynamics of coastal waters and river plumes as well as particles in suspension, which are advected away from the coast (Figure 4.15 top left). The difference in autumn lies in the extent of the river plumes and the meandering of the submesoscale structures (Figure 4.14 bottom). Lower wind amplitude is recorded and the river runoffs regime is 10 times less compared to winter (Figure 4.17). According to *Capet et al., 2008*, when submesoscale fronts become unstable, another stage of frontogenesis is generated at the interface of submesoscale meanders, which leads to the formation of small-scale filaments (Figure 4.14

bottom left). In fact, *Ferrari, R.(2011)* suggest that the instability causes the less dense water to superimpose on the denser water causing the plume to stabilize, thus closing the pathway between air-sea interactions, and this situation is more likely to occur when river runoffs or intensity of winds are low.

The strong gradient observed on the singularity image in February is indicative of stronger submesoscale frontogenesis which coincides with the chlorophyll-*a* imagery, while in autumn the magnitude of the fronts are uniform and widespread throughout the domain. Indeed, both seasons are skewed-right indicating strong frontal activities. Consequently, it can be deduced that large freshwater discharges and dominant winds explain the higher skewness value obtained in winter compared to autumn. Although the spectral slope is slightly higher in winter compared to autumn, there are no distinct differences in distinguishing between the two seasons.

5.3 Interannual and Seasonal Variability over the whole period

After analyzing the short time scales and seasonal variability of the different variables, the last approach is to investigate how the hydrodynamic processes occur on interannual variations between the period 2003 and 2013. The graph of the river runoffs (Figure 4.20) indicates a seasonal trend; high river outflow regime in winter compared to low rate of river runoffs in summer. High peaks were observed in 2003, 2004, 2006, 2007 and 2013 often exceeding $3000 m^3 s^{-1}$. However, the rate of river runoffs in summer 2007 and 2008 appears to be higher than the mean annual flow during the same period. The mean chlorophyll-*a* concentration (Figure 4.21) was plotted for cloud-free images only and for the same time period as river runoffs. A seasonal cycle was also noted revealing high mean chlorophyll-*a* value in winter seasons in comparison to summer. Accordingly, the high peaks noted in 2004, 2006, 2007, 2008 and 2012 are periods of phytoplankton blooms occurring particularly in spring. As observed on the mean chlorophyll-*a* plot, the concentration for summer 2007 and 2008 are found to be higher than the mean annual value during this period. From a visual perspective, high mean chlorophyll-*a* concentration appears to coincide with the high river runoffs.

The skewness values for all clear images were also plotted for the whole time series (Figure 4.23) and a high interannual variability is noted. It was observed that positive skewness is

predominant in winter compared to negative skewness in summer. This implies that stronger frontal structures are present in winter and vice versa in summer. An anomaly is observed in 2008 showing positive skewness during the summer season and this feature coincides with the high rate of river runoff observed for the same period. However, it should be noted that the graph is not perfectly symmetrical due to a lack of cloud-free images for the whole time series. The interannual variability in the wind intensity was also analyzed but for the period 2006 to 2013 (Figure 4.22) and no significant differences are observed among the years. A distinct seasonal trend was observed showing high wind intensity reaching 7.5 m s^{-1} in winter while having a lower magnitude of about 3.5 ms^{-1} in summer. In fact it can be deduced that positive skewness is correlated with high river runoffs and high wind intensity. In summary, frontal dynamics at submesoscales are largely driven by interactions between the magnitude of river discharge as well as wind influence.

Chapter 6 Conclusions and Perspectives

The main objectives of this thesis were to: 1) Identify and investigate submesoscale structures in the Bay of Biscay, more precisely at the mouth of Loire River. 2) Study the impact of winds and river runoffs on the circulation of the plumes; submesoscales dynamics. 3) Apply statistical methods to highlight and characterize these features.

Previous studies *(Sharples and Simpson, 1993, Lagadeuc et al., 1997)* have suggested through observations and models that frontal activity on the shelf is commonly found in regions of freshwater influence (ROFIs). Consequently, our study was to focus on the turbulence induced by river plume dynamics. Remotely-sensed images of Chlorophyll-*a* concentration, Sea Surface temperature and Suspended Particulate Matters were analyzed to identify submesoscale features and observe how they evolve with time and space. Chlorophyll-*a* provides a useful proxy indicator compared to other ocean scalars to monitor the movement of phytoplankton biomass. However, the inconvenience was that very few images (60 images per year) were available at the appropriate time and space scales over the 10 year (2003-2013) study period.

Other hydrodynamic parameters like winds and river runoffs have been studied to analyze what impact they have on the submesoscale dynamics. It was observed that the evolution of low salinity water changes seasonally; maximum river runoffs and south-westerly winds (downwelling) in winter drive the plumes northwards, while reduced river discharges and north-westerly winds in spring extend the plumes offshore *(Lazure et al., 1998)*. Singularity exponents, generated from chlorophyll-*a* concentration images, were used to highlight and sort frontal activity. It was noted that the submesoscale structures were ubiquitous *(Capet et al., 2008)* and spread widely throughout the whole domain. However, depending on the season, the frontal structures vary in intensity due to river outflow regime and the influence of winds; stronger frontal gradients in winter and vice versa in summer.

The probability density function (skewness calculated on singularity exponents) is one of the statistical methods used to characterize submesoscale structures. The study shows that during

winter, the PDF curve is skewed-right, implying that the frontal structures are stronger compared to summer (skewed-left). It is therefore deduced that the intense submesoscale activity in winter is due to the high river runoffs and dominant winds. Spectral analysis is the other method used to characterize the submesoscale structures, but the results displayed no significant differences in frontal spatial scales with time and do not coincide with other studies (Capet et al., 2008, Klein et al., 2008). This might be due to the small domain chosen for analysis or because the density difference across the submesoscale fronts is much smaller compared to other studies made on the Gulf stream or the California current system.

Future Works

There are several avenues for extending this work:

- ✓ The priority for the next step would be to analyze other rivers like the Gironde (Fig 6.1).

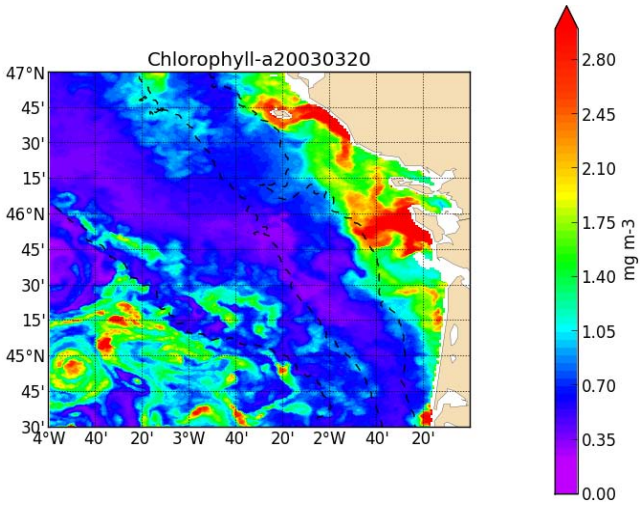

Fig 6. 1 Satellite image of Chlorophyll-*a* concentration for the Gironde River showing meso and sub-mesoscale activities close to the river mouth in spring.

- ✓ Results could be further developed using a new indicator of PDF statistics. E.G by setting up a threshold value at the zero mark and calculating the area under the curve on the right or left hand of the red line (Fig 6.2).

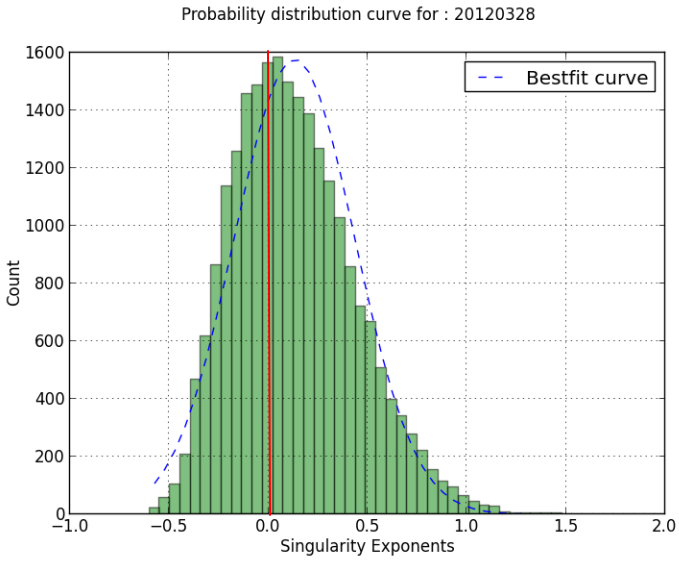

Fig 6. 2 Probability density function curve indicating threshold mark

- ✓ The spectral analysis could be performed on a larger domain to check whether the spectral slope agrees with other studies made.

- ✓ A correlation method could be applied to calculate the significance level between the interannual graphs (intensity of winds or rate of river runoffs against skewness values).

- ✓ Exploring other available *in situ* data (e.g. island network, cruise sections and future experiments)

- ✓ Using a model would enable a detailed investigation into the formation of submesoscale features and processes influencing the submesoscale dynamics in the Bay of Biscay.

Bibliography

Batifoulier, F., Lazure, P. & Bonneton, P., 2012. Poleward coastal jets induced by westerlies in the Bay of Biscay. *Journal of Geophysical research,* Volume 117, p. C03023.

Bergeron, J.-P. & Koueta, N., 2011. Biological productivity enhancement over a continental shelf break (Bay of Biscay, NE Atlantic). *Journal of Oceanography,* Volume 67, Number 2, pp. 249-252.

Boccaletti, G., Ferrari, R. & Fox-Kemper, B., 2007. Mixed Layer Instabilities and Restratification. *Journal of Physical Oceanography,* Volume 37, pp. 2228-2250.

Capet, X., Mcwilliams, J., Molemaker, M. & Shchepetkin, A., 2008b. Mesoscale to submesoscale transition in the California Current System. Part II: Frontal processes. *Journal of Physical Oceanography,* Volume 38, pp. 44-64.

Capet, X., Mcwilliams, J., Molemaker, M. & Shchepetkin, A., 2008a. Mesoscale to Submesoscale Transition in the California Current System.Part I: Flow Structure, Eddy Flux, and Observational Tests. *Journal of Physical Oceanography,* Volume 38, pp. 29-43.

Capet, X., Mcwilliams, J., Molemaker, M. & Shchepetkin, A., 2008c. Mesoscale to Submesoscale Transition in the California Current System.Part III: Energy Balance and Flux. *Journal of Physical Oceanography,* Volume 38, pp. 2256-2269.

Charney, J., 1971. Geostrophic turbulence. *Journal of Atmospheric Science,* Volume 28, pp. 1087-1095.

Charria, G. et al., 2013. Surface layer circulation derived from Lagrangian drifters in the Bay of Biscay. *Journal of Marine Systems,*Volume 109-110, pp.S60-S76.

Cloern, J. & Jassby, A., 2010. Patterns and Scales of Phytoplankton Variability in Estuarine- Coastal Ecosystems. *Estuaries and Coasts ,* Volume 33, pp. 230-241.

Cloern, J. E., 2001. Our evolving conceptual model of the coastal eutrophication problem. *Marine Ecology Progress Series,* Volume 210, pp. 223-253.

Cloern, J., 1996. Phytoplankton bloom dynamics in coastal ecosystems: A review with some general lessons from sustained investigation of San Francisco Bay, California. *Reviews of Geophysics,* Volume 34, pp. 127-168.

Cravo, A. et al., 2006. Impact of outflow from the Guadiana River on the distribution of suspended particulate matter and nutrients in the adjacent coastal zone. *Estuarine Coastal Shelf Science,* Volume 70, pp. 63-75.

Denman, K. & Abott, M., 1994. Time scales of pattern evolution from cross-spectrum analysis of advanced very high resolution radiometer and coastal zone color scanner imagery. *Journal of Geophysical Research,* Volume 99, pp. 7433-7442.

Déqué, M., Dreveton, C., Braun, A. & Cariolle, D., 1994. The ARPEGE-IFS atmosphere model : a contribution to the French community climate modeling. *Climate Dynamics,* Volume 10, pp. 249-266.

Ferrari, R., 2011. A frontal challenge for climate models, *Science,* Volume 332, pp. 316-317.

Ferrer, L. et al., 2009. Low-salinity plumes in the oceanic region of the Basque Country. *Continental shelf Research,* Volume 29, pp. 970-984.

Fox-Kemper, B. & Ferrari, R., 2008. Parameterization of mixed layer eddies. Part II: Prognosis and impact. *Journal of Physical Oceanography,* Volume 38(6), pp. 1166-1179.

(a) Fox-Kemper, B., Ferrari, R. & Hallberg, R., 2008. Parameterization of mixed layer eddies. Part I: Theory and diagnosis. *Journal of Physical Oceanography,* Volume 38, pp. 1145-1165.

Gohin, F. et al., 2003. Satellite and in situ observations of a late winter phytoplankton bloom in the Northen Bay of Biscay. *Continental Shelf Research,* Volume 23, pp. 1117-1141.

Gohin, F. et al., 2005. Satellite-derived parameters for biological modelling in coastal waters: Illustration over the eastern continental shelf of the Bay of Biscay. *Remote Sensing of Environment,* Volume 95(1), pp. 29-46.

Gohin, F., Druon, J. & Lampert, L., 2002. A five channel chlorophyll concentration algorithm applied to Sea WIFS data processed by SeaDAS in coastal waters. *International Journal of Remote Sensing,* Volume 23(8), pp. 1639-1661.

Gower, J., Denman, k. & Holyer, R., 1980. Phytoplankton patchiness indicates the fluctuation spectrum of mesoscale oceanic structure. *Nature,* Volume 288, pp. 157-159.

Haine, T. W. N and Marshall, J.C (1998), Gravitational, symmetric, and baroclinic instability of the ocean mixed layer, J. Phys. Oceanogr., 28, 634–658.

Hoskins, B., 1982. The mathematical theory of frontogenesis. *Annu Rev. Fluid Mechanics,* Volume 14, pp. 131-151.

Isern-Fontanet, J., Turiel, A., Garcia-Ladona, E. & Font, J., 2007. Microcanonical multifractal formalism: application to the estimation of ocean surface velocities. *Journal of Geophysical Research,* Volume 112, pp. X-1-X-19.

Jégou, A. & Lazure, P., 1995. Quelques aspects de la circulation sur le plateau atlantique.Actas del IV Coloquio internacional sobre Oceanografia del Golfo de Vizcaya. *Instituto Espanol de Oceanografia,* pp. 99-106.

Klein, p. et al., 2008. Upper ocean turbulence from high-resolution 3D simulations. *Journal of Physical Oceanography,* Volume 38(8), pp. 1748-1763.

Koutsikopoulos, C. & Le Cann, B., 1996. Physical processes and hydrological structures related to the Bay of Biscay anchovy. *Scientia Marina,* Volume 60, pp. 9-19.

Lagadeuc, Y., Boule, M. & Dodson, J., 1997. Effect of vertical mixing on the vertical distribution of copepods in coastal waters. *Journal of Plankton Research,* Volume 19, pp. 1183-1204.

Lapeyre, G., Klein, P. & Hua, B. L., 2006. Oceanic Restratification Forced by surface frontogenesis. *Journal of physical Oceanography,* Volume 36, pp. 1577-1590.

Lazure, P. & Jégou, A., 1998. 3D modelling of seasonal evolution of Loire and GIronde plumes on Biscay Bay continental shelf. *Oceanologica Acta,* Volume 21, pp. 165-177.

Lazure, P., Dumas, F. & Vrignaud, C., 2008. Circulation on the Armorican shelf (Bay of Biscay) in autumn. *Journal of Marine Systems,* Volume 72, pp. 218-237.

Le Boyer, A. et al., 2013. Circulation on the shelf and the upper slope of the Bay of Biscay. *Continental Shelf Research,* Volume 55, pp. 97-107.

Le Cann, B. & Pingree, R., 1995. Circulation dans le golfe de Gascogne: une revue de travaux recentes.. *Actas del IV Coloquio Internacional sobre Oceanografia del Golfo de Viscaya,* pp. 217-234.

Le Cann, B., 1982. *Evolution annuelle de la structure hydrologique du plateau continental au sud de la Bretagne: Modélisation numérique.*Thèse 3e cycle en océanographie physique. Université de Bretagne Occidentale (France).

Legg, S. & McWilliams, J., 2001. Convective modifications of a geostrophic eddy field. *Journal Physical Oceanography,* Volume 31, pp. 874-891.

Lévy, M. et al., 2012. Bringing Physics to life at the submesoscale. *Geophysical Research Letters,* 39, L14602, doi:10.1029/2012GL052756)

Lévy, M., Klein, P. & Tréguier, A., 2001. Impacts of submesoscale physics on production and subduction of phytoplankton in an oligotrophic regime. *Journal of Marine Research,* Volume 59, pp. 535-565.

Lihan, T. et al., 2011. Influence of River Plume on Variability of Chlorophyll-a concentration using Satellite Images.. *Journal of Applied Sciences,* Volume 11, pp. 484-493.

Lunven, M. et al., 2005. Nutrient and phytoplankton distribution in the Loire River plumes (Bay of Biscay, France) resolved by a new Fine Scale Sampler. *Estuarine, Coastal and Shelf Science,* Volume 65(1-2), pp. 97-108.

Munk, W., Armi, L., Fischer, K. & Zachariasen, Z., 2000. Spirals on the sea. Proc.Roy.Soc. London, Volume 456A, pp. 1217-1280.

Nieves, V. et al., 2007. Common turbulent signature in sea surface temperature and chlorophyll maps. *Geophysical Research Letters,* Volume 34, p. L23602.

Petus, C. et al., 2010. Estimating turbidity and total suspended matter in the Adour RIver plume (South Bay od Biscay) using MODIS 250-m imagery. *Continental shelf research,* Volume 30(5), pp. 379-392.

Pichon, A. & Correard, S., 2006. Internal tides modelling in the Bay of Biscay.Comparisons with observations. *Sci Mar,* Volume 70, pp. 65-88.

Pingree, R. & Le Cann, B., 1989. Celtic and Armorican slope and residual currents. *Progress in Oceanography,* Volume 23, pp. 303-338.

Pingree, R. & Le Cann, B., 1992. Three anticyclonic Slope Water Oeanic Eddies (SWODDIES) in the Souther Bay of Biscay in 1990. *Deep-Sea Research,* Volume 39(7/8), pp. 1147-1175.

Puillat, I. et al., 2004. Hydrological variability on the French continental shel in the Bay of Biscay, during the 1990s. *Continental Shelf Research,* Volume 24, pp. 1143-1163.

Puillat, I. et al., 2006. Mesoscale hydrological variability induced by northwesterly wind on the French continental shelf of the Bay of Biscay. *Scientia Marina,* Volume 70, pp. 15-26.

Rivier, A., Gohin, F. & Bryere, P., 2012. Observed vs. predicted variability in non-algal suspended particulate matter concentration in the English Channel in relation to tides and waves.. *Geo-Mar Lett,* Volume 32, pp. 139-151.

Rudnick, D., 2001. On the skewness of vorticity in the upper ocean. *Geophysical Research Letters,* Volume 28, pp. 2045-2048. BIBLIOGRAPHY \l 1033

Sharples, J. & Simpson, J., 1993. Periodic frontogenesis in regions of freshwater influence. *Estuaries,* Volume 16(1), pp. 74-82.

Signoret, M., Monreal-Gomez, M., Aldeco, J. & Salas-de-Leon, D., 2006. Hydrography, oxygen saturation, suspended particulate matter and chlorophyll-a fluorescence in an oceanic region under freswater influence. *Estuarine Coastal Shelf Science,* Volume 69, pp. 153-164.

Spall, M., 1995. Frontogenesis, subduction and cross-front exchange at upper ocean fronts. *Journal of Geophysical Research,* Volume 100, pp. 2543-2557.

Spall, M., 1997. Baroclinic jets in confluent flow. *Journal of Physical Oceanography,* Volume 27(6), pp. 1054-1071.

Spall, S. & Richards, K., 2000. A numerical model of mesoscale frontal instabilities and plankton dynamics - l. Model formulation and initial experiments. *Deep Sea Research,* Volume 47, pp. 1261-1301.

Taylor, J. & Ferrari, R., 2011. Ocean fronts trigger high latitude phytoplankton blooms. *Geophysical research Letters,* 38(23), p. DOI:10.1029/2011GL049312.

Thomas, L. & Ferrari, R., 2008. Friction, frontogenesis and the stratification of the surface mixed layer. *Journal of Physical Oceanography,* Volume 38, pp. 2501-2518.

Thomas, L. & Lee, C., 2005. Intensification of ocean fronts by down-front winds. *Journal of Physical Oceanography,* Volume 35, pp. 1086-1102.

Thomas, L., 2005. Destruction of potential vorticity by winds. *Journal of Physical Oceanography,* Volume 35, pp. 2457-2466.

Thomas, L., Tandon, A. & Mahadevan, A., 2008. Submesoscale processes and dynamics. In M.W.Hetcht and H.Hasumi (Eds.), Ocean Modeling in an Eddying Regime, Geophysical Monograph Series. *American Geophysical Union, Washigton DC,* Volume 177, pp. 17-38.

Turiel, A. & Parga, N., 2000. The Multifractal Structure of Contrast Changes in Natural Images: From Sharp Edges to Textures. *Neural computation,* Volume 12, No.4, pp. 763-793.

(a)Turiel, A. et al., 2008. Microcanonical Multifractal Formalism: a geometrical approach to multifractal systems. Part I: Singularity Analysis. *Journal of Physics,* Volume 41, p. 015501.

Turiel, A., Nadal, J. & Parga, N., 2003. Orientational minimal redundancy wavelets : from edge detection to perception. *Vision Research,* Volume 43, pp. 1061-1079.

(b)Turiel, A. et al., 2008. Tracking oceanic currents by singularity analysis of Microwave Sea Surface Temperature images. *Remote Sensing of Environment,* Volume 112, pp.2246-2260

Vincent, A. & Kurc, G., 1969. Hydrologie, variations saisonnières de la situation thérmique du golfe de Gascogne en 1967. *Revue des Travaux de l'institut des Peches Maritimes,* Volume 33, pp. 79-76.

Wang, D., 1993. Model of frontogenesis: Subduction and upwelling. *Journal of Marine research,* Volume 51, pp. 497-513.

Yahia, H., Sudre, J., Pottier, C. & Garçon, V., 2010. Motion analysis in oceanographic satellite images using multiscale methods and the energy cascade. *Pattern Recognition,* Volume 43(10), pp. 3591-3604, Elsevier(2010).

Yoshikawa, Y., Akitomo, K. & Awaji, T., 2001. Formation process of intermediate water in baroclinic current under cooling. *Journal of Geophysical Research,* Volume 106, pp. 1033-1051.

Websites visited:

MODIS instrument - *http://modis.gsfc.nasa.gov/data/*

http://oceancolor.gsfc.nasa.gov/cgi/browse.pl?sen=am

Implementation of SST Processing within the OBPG - *http://oceancolor.gsfc.nasa.gov/DOCS/modis_sst*

Singularity exponents - *http://cp34-bec.cmima.csic.es/new-singularity-exponent-products-now-available/*

Skewness - *http://en.wikipedia.org/wiki/Skewness*

http://www.hydro.eaufrance.fr/

Group for High Resolution Sea Surface Temperature - *https://www.ghrsst.org/*

Bay of Biscay - http://www.eoearth.org/view/article/150448/

Detecting chlorophyll - *http://www.kikiwi.fr/uploads/data/Mesures/Fluorimetre/FluorimetreTenum.pdf*

(b) Fox-Kemper.B., Danabasoglu.G., Ferrari.R., Hallberg.R.W., 2008. Parameterizing Submesoscale Physics in Global Climate Models. *CLIVAR Exchanges.*Volume 13 No., pp.3-5 (*http://www.gfdl.noaa.gov/bibliography/related_files/bfk0801.pdf)*

Jacobs.G.A, NRL, Stennis Space Center, MS; and Spence.P, Bartels.B and Bub.F.L. 2013.Conditional Predictability in Assimilation: Ocean Frontogenesis Filaments. *(https://ams.confex.com/ams/93Annual/webprogram/Paper221140.html)*

http://www.photosynthesis.ch/fluorescence.htm

APPENDIX A

Turbulence Regime

A.1 Turbulence Regime

As quoted in McDonough, 2004, 2007 "Turbulence is any chaotic solution to the 3-D Navier-Stokes equations that is sensitive to initial data and which occurs as a result of successive instabilities of laminar flows as a bifurcation parameter is increased through a succession of values".[9]

Turbulence flows have the following characteristics[9]:

- ✓ Disordered and always chaotic
- ✓ Three-dimensional, rotational and non-zero vorticity
- ✓ Large range of length and time scales
- ✓ Intermittency in space and time
- ✓ Diffusivity leads to rapid mixing, increased momentum, heat and mass transfer rates.
- ✓ Associated with high Reynolds numbers.

The schematic diagram below indicates the transition steps a flow will undergo to reach its chaotic state[9].

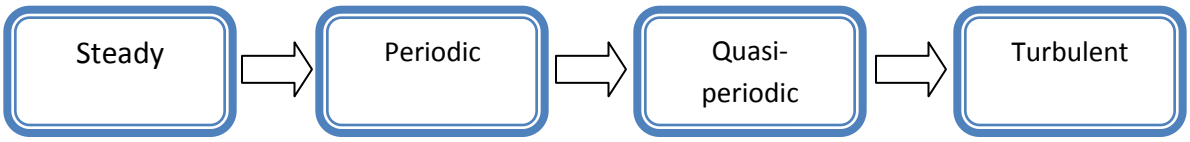

A.2 Inertial Cascade Ranges:

Figure A.1 shows a typical energy spectrum having an inertial range of wavenumbers, as a log-log plot. It is known as the turbulent energy cascade whereby energy is neither produced nor dissipated but is transferred to smaller scales. This energy is analogous to the second law of thermodynamics in view of increasing the entropy of the universe.

Turbulent flows transfer energy from the forced wavenumbers, by irregular mode interactions to other dissipative modes. The Kolmogorov 1941 theory described turbulence at small scales and

[9] Lectures in Computational Fluid Dynamics of Incompressible Flow: Mathematics, Physics and Algorithms (http:// www.engr.uky.edu/~acfd) by McDonough 2004, 2007.

the objective was to represent the process of turbulent flow mathematically for 3-D hydrodynamic turbulence. The first step was taken by Richardson, 1922 who characterized turbulence as a cascade of eddies. Large eddies are formed by the forcing mechanism where they are then broken down into smaller eddies because they are unstable. These eddies continue to break down into smaller eddies until they become sufficiently small, stable and dissipate the incoming energy into heat. The length scale, $L_{o,}$ of the large eddies formed by the forcing mechanism is known as the integral length scale. The length scale, $L_d = 1/k_{d,}$ of the small eddies that dissipate into heat is called the Kolmogorov microscale and the length scale, L, is in the inertial range, where $L_d < L < L_{o.}$ [9]

The 2D cascade theory is homologous to Kolmogorov's spectrum of the form $\mathbf{E} \propto k^{-5/3}$, with the cascade rate being independent of the spatial scale for which $L_d < L < L_o$ *(Kraichnan, 1967 as cited on ucla website[10]).* There are 2 possible inertial cascade ranges for 2D turbulence that separates the dissipative and larger scales[10]:

(i) Inverse energy inertial cascade energy, where ε, is the scale-independent cascade rate toward **large scales**,

$$\mathbf{E\ (k) \sim\ } \varepsilon^{\frac{2}{3}} \boldsymbol{k}^{\frac{-5}{3}} \qquad \mathbf{(4)}$$

(ii) Forward enstrophy inertial cascade range, where $\hat{\eta}$ is the scale-independent cascade rate toward the **smaller scales**,

$$\mathbf{E\ (k) \sim} \hat{\boldsymbol{\eta}}^{\frac{2}{3}} \boldsymbol{k}^{-3} \qquad \mathbf{(5)}$$

The cascade of enstrophy to small scales relates to a transition to the enstrophy dissipation range at a scale L_d defined by:

$$\mathbf{L_d} = \left(\frac{\boldsymbol{\nu}^3}{\hat{\boldsymbol{\eta}}}\right)^{\frac{1}{6}} \qquad \mathbf{(6)}$$

Which is analogous to the Kolmogorov's dissipation length in 3D homogenous turbulence.

[10] http://www.atmos.ucla.edu/~jcm/turbulence_course_notes/

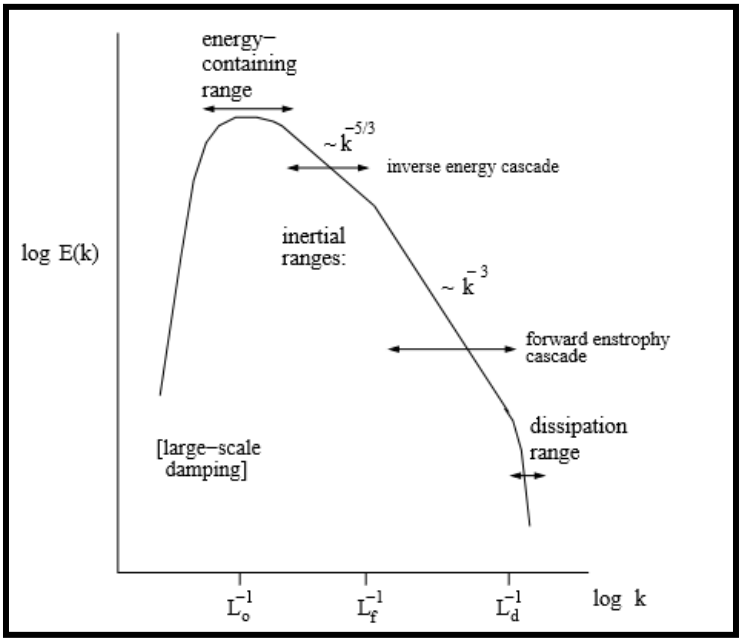

Fig A. 1 A schematic kinetic energy spectrum in equilibrium two-dimensional homogeneous turbulence and L_f being the intermediate scale. ***(Source:*** ***http://www.atmos.ucla.edu/~jcm/turbulence_course_notes/)***

APPENDIX B

Singularity Exponents

B.1 Calculating Singularity exponents

The objective of using singularity analysis is to obtain at each domain point, a dimensionless measure called the singularity exponent of the degree of regularity and irregularity of a signal at each domain point. The singularity exponent is an extension of the classical formulation (differentiation) whereby the degree of regularity of a signal Y at the point $\vec{z}$ is measured by the Hölder exponent, H($\vec{z}$). The latter comes from a pseudo-Taylor expansion[11]:

$$Y(\vec{z}+\vec{r}) - Y(\vec{z}) \approx \alpha(\vec{z}) r^{H(\vec{z})}, \; r \ll 1 \qquad \textbf{(7)}$$

Where, the displacement $\vec{r}$, is very small. The size r is controlled by the power-law defined by the singularity exponent H($\vec{z}$).

When H($\vec{z}$) =1 : once differentiable

H($\vec{z}$) =2 : double differentiable

H($\vec{z}$) =0 : continuous

0<H($\vec{z}$)<1 : The function is more regular than a continuous function but do not allow differentiation.

Obtaining singularity exponent from observations is a complicated task due to the presence of noise that alters the value of the exponent. As such, discrete data must be interpolated on the continuum of scales in order to obtain the proper power-law scaling[11] given in equation **(7).**

To avoid these issues, wavelet projections of the data was used. The wavelet projection of the gradient is defined by the scalar signal Y at the point **z** and scale **r** as shown in equation **(8):**

$$T_{\phi} Y(\mathbf{z}, r) \equiv \int d\boldsymbol{x}\, Y(\boldsymbol{x}) \frac{1}{r^d} \phi\left(\frac{\mathbf{z}-\mathbf{x}}{\mathrm{r}}\right) \qquad \textbf{(8)}$$

[11] Turiel, A. et al., 2008. Tracking oceanic currents by singularity analysis of Microwave Sea Surface Temperature images. *Remote Sensing of Environment,* Volume 112, pp.2246-2260

Where d represents the dimension of signal domain (d=2 for ocean's surface). Wavelet projections are continuous wavelet transforms that are primarily used for analysis. They are able to transmit much information and are adapted to detect any change in the data (Turiel et al., 2008).

According to Turiel et al., 2008, if the scalar signal Y has a singularity exponent H(**z**) at the point **z** and if the wavelet is such that the wavelet transforms of any polynomial with large order vanishes, then:

(9)

Where $o\left(r^{H(\mathbf{z})}\right)$ indicate that it is negligible compared to $r^{H(\mathbf{z})}$. However, H(**z**) is dimensionless and it is a measure of the degree of regularity or irregularity of a function around the point z.

According to *Turiel et al., 2006,* singularity exponents obtained when applying directly the wavelet analysis results in a poor resolution compared to that applied to discretized data. However, when performing a wavelet projection of the modulus of the gradient, this results to a more precise determination and enhanced resolution of the singularity exponents **(Step 2 in Figure B.1)**.

The wavelet projection of the modulus of the signal is given by:

(10)

The signal is then decomposed into fractal components called multifractal decomposition, where each component is attributed to a singularity exponent value.

The wavelet,ϕ, is a numerical implementation of the Lorentzian wavelet (Turiel et al.,2008) given by:

(11)

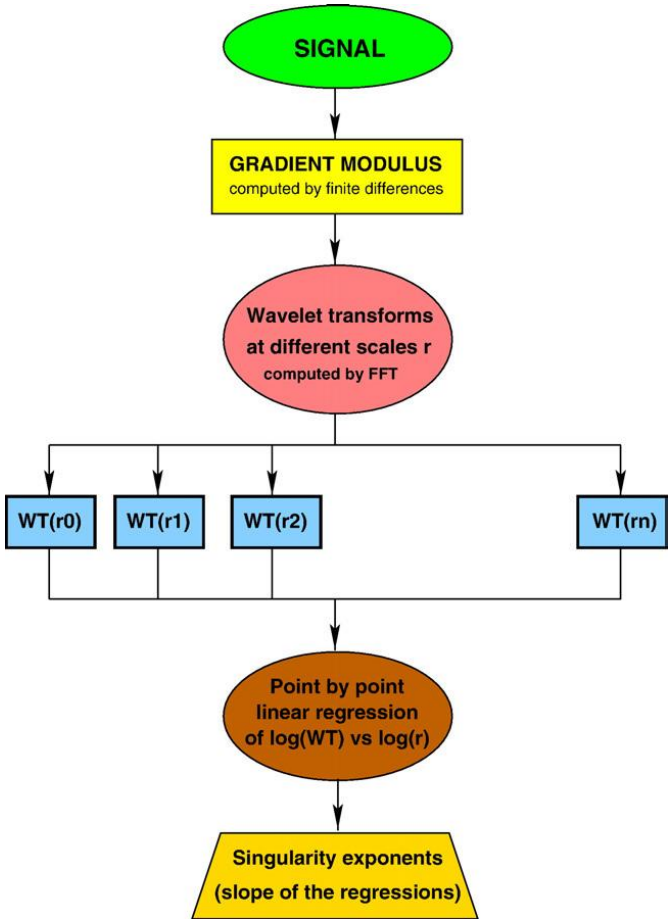

Fig B. 1 Schematic representation of an algorithm to calculate the singularity exponents of a signal. ***(Turiel et al., 2008[11])***

APPENDIX C

Consecutive images of chlorophyll-a concentration

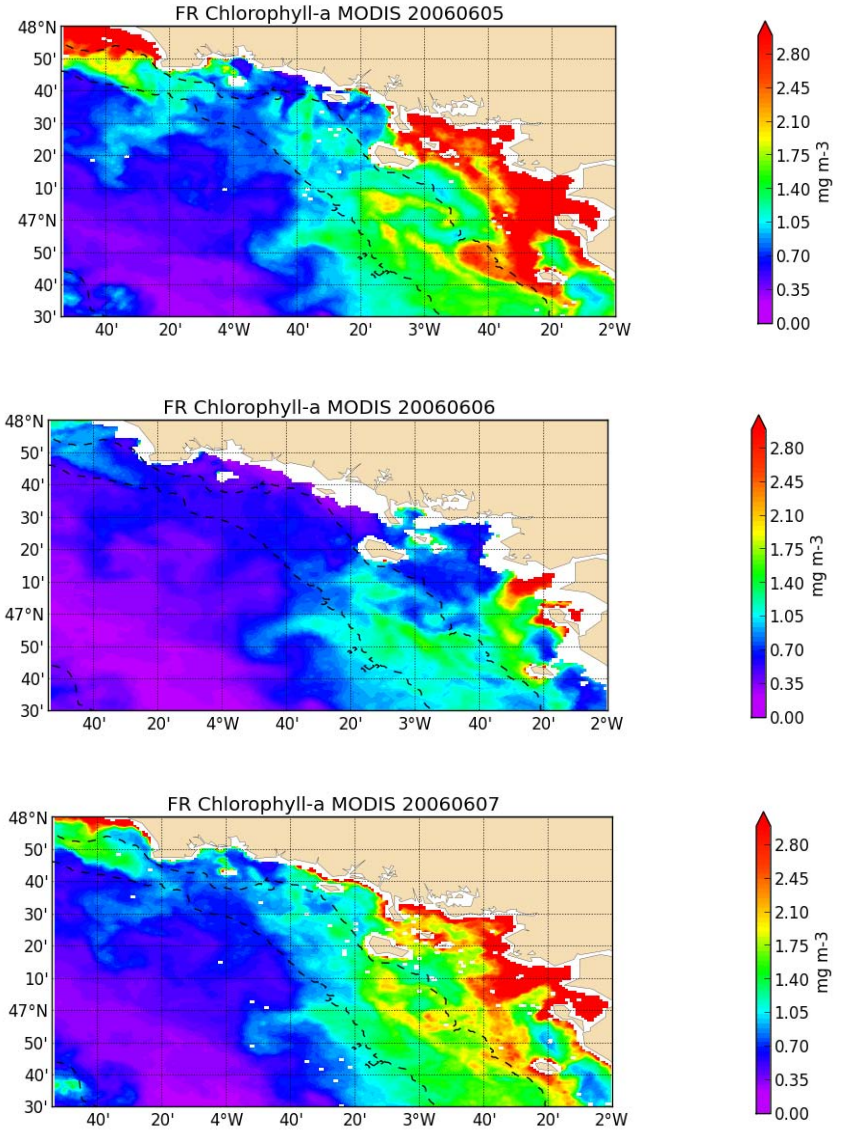

Fig C. 1 Satellite images of chlorophyll-*a* concentration for three consecutive days in June 2006 (a – 05/06/2006, b – 06/06/2006, c – 07/06/2006) showing similar event as October 2008 described in section 4.2.1.

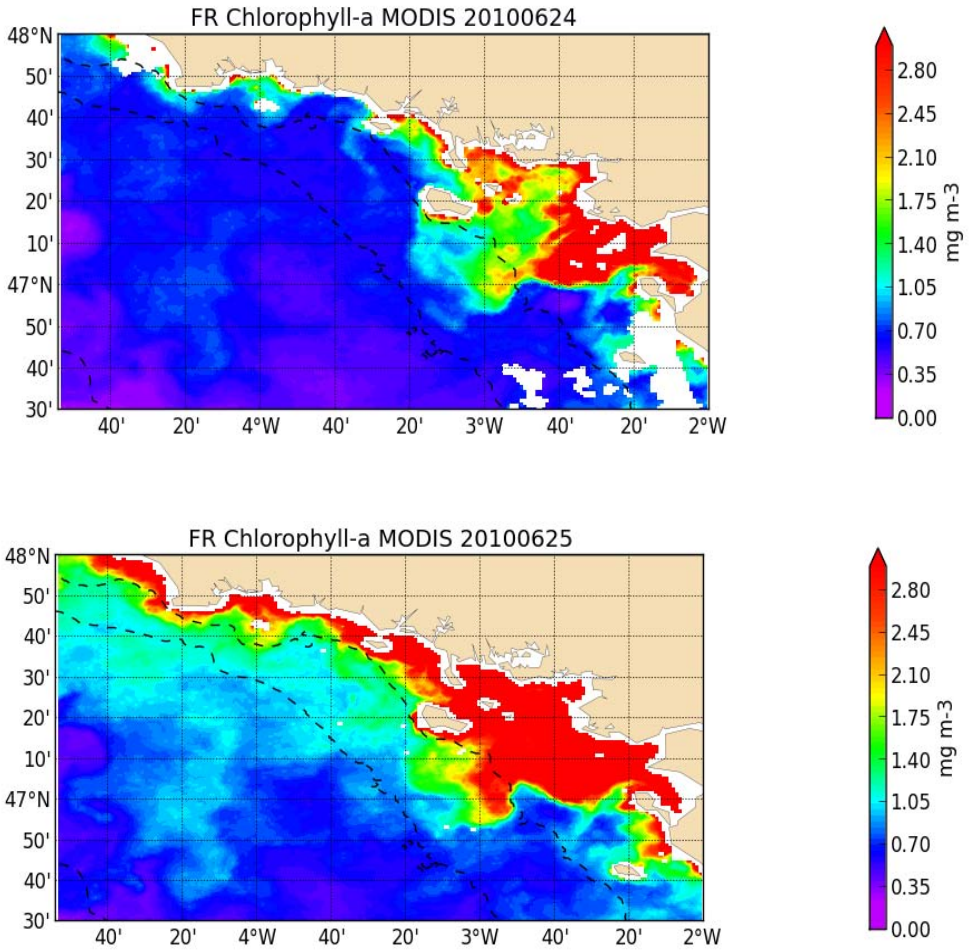

Fig C. 2 Satellite images of chlorophyll-*a* concentration for two consecutive days in June 2010 (a – 24/06/2010, b – 25/06/2010) showing similar event as October 2008 described in section 4.2.1.

APPENDIX D

Spectral Slope

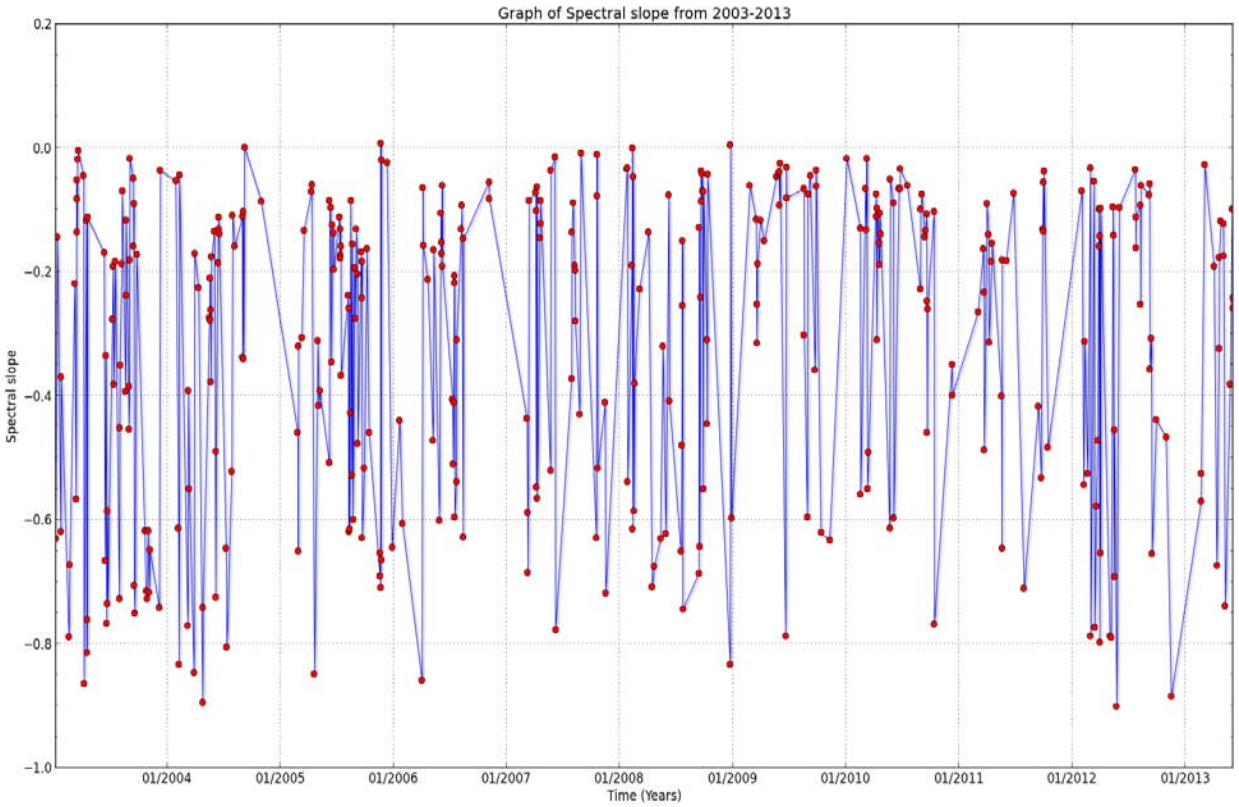

Fig D. 1 Values of spectral slope for cloud-free images plotted on a 10-year dataset (2003-2013) showing no seasonal variability.